GEOPHYSICS, VOL. 81, NO. 6 (NOVEMBER-DECEMBER 2016); P. C337–C354, 19 FIGS., 1 TABLE.
10.1190/GEO2016-0138.1

A separable strong-anisotropy approximation for pure qP-wave propagation in transversely isotropic media

Jörg Schleicher[1] and Jessé C. Costa[2]

ABSTRACT

The wave equation can be tailored to describe wave propagation in vertical-symmetry axis transversely isotropic (VTI) media. The qP- and qS-wave eikonal equations derived from the VTI wave equation indicate that in the pseudoacoustic approximation, their dispersion relations degenerate into a single one. Therefore, when using this dispersion relation for wave simulation, for instance, by means of finite-difference approximations, both events are generated. To avoid the occurrence of the pseudo-S-wave, the qP-wave dispersion relation alone needs to be approximated. This can be done with or without the pseudoacoustic approximation. A Padé expansion of the exact qP-wave dispersion relation leads to a very good approximation. Our implementation of a separable version of this equation in the mixed space-wavenumber domain permits it to be compared with a low-rank solution of the exact qP-wave dispersion relation. Our numerical experiments showed that this approximation can provide highly accurate wavefields, even in strongly anisotropic inhomogeneous media.

INTRODUCTION

Reverse time migration (RTM) using anisotropic velocity models has become the standard methodology for seismic imaging in complex exploration settings. Although anisotropy is essentially an elastic property, migration with an elastic wave equation is currently unfeasible. Even if one is able to successfully estimate elastic migration velocity models, the computational cost to solve the elastic wave equation and the lack of efficient algorithms to compute wavemode separation are major obstacles to elastic imaging. In this scenario, a pseudoacoustic approximation (Alkhalifah, 1998, 2000) is a very cost-effective approach to anisotropic RTM. The pseudoacoustic wave equation, proposed to model the evolution of qP-modes, is derived under the assumption that shear velocity is zero along the symmetry axis.

However, finite-difference implementations of a pseudoacoustic wave equation can be plagued by physical instability and undesirable S-wave modes even in the weakly anisotropic regime. Several strategies have been proposed to overcome these problems. Stability of space-time FD implementations of the pseudoacoustic wave equation can only be assured if the Thomsen's parameters satisfy the constraint $\epsilon \geq \delta$, which is not always valid for shales (Thomsen, 1986). Fletcher et al. (2009) and Fowler et al. (2010) show that a stable approximation for qP-modes in VTI media can be derived, if one does not assume the shear velocity along the symmetry axis to be zero. However, their proposed stable coupled system of second-order differential equations still can produce undesirable S-wave modes.

The mitigation of the S-wave in FD implementations of the pseudoacoustic approximation has been an area of active research since the original work of Alkhalifah (1998). For example, Alkhalifah (2003) indicates that if the source is in an isotropic region, the S-modes are not generated, although it still can be produced at interfaces with sharp contrast. The work of Grechka et al. (2004) indicates that the instability of a pseudoacoustic wave equation is due to the coupling of the S-mode to the qP-mode. The S-mode is not stable, when $\epsilon \geq \delta$. Other removal strategies include the choice of a finite S-wave velocity (Fletcher et al., 2009) to achieve a zero S-wave reflection coefficient everywhere in the model. However, this introduces an additional parameter and is hard to generalize to orthorhombic media. The propagation filter of Le and Levin (2014) is cumbersome because it requires eigenvalue decomposition.

For this reason, a very successful solution to obtain a stable qP-wave equation is to factor out these spurious modes from the pseudoacoustic wave equation. The work of Klíe and Toro (2001) presents one such approximation for a pure qP-wave equation under the assumption of weak anisotropy. Exact factorization results in a pseudodifferential operator in the mixed space-wavenumber do-

Manuscript received by the Editor 14 March 2016; revised manuscript received 7 June 2016; published online 1 November 2016.
[1]University of Campinas (Unicamp), Institute of Mathematics, Statistics, and Cientific Computation (IMECC), Department of Applied Mathematics (DMA), Campinas, Brazil. E-mail: js@ime.unicamp.br.
[2]Federal University of Pará (UFPA), Faculty of Geophysics (FaGeo), Belém, Brazil. E-mail: jesse@ufpa.br.

main (Liu et al., 2009). Differential equations in space and time for the pure qP-mode can be derived through approximations to the exact pseudodifferential operator for qP evolution. Liu et al. (2009) propose an algorithm to implement the exact factorization of the pseudoacoustic wave equation in the mixed space-wavenumber domain.

Pestana et al. (2012) derive an alternative approximation for the exact factorization, which is valid for weak anisotropy and can be implemented using finite difference in time and pseudospectral method in space. Zhan et al. (2013) show how to generalize this implementation to tilted transversely isotropic (TTI) media. More sophisticated approximations of this factorization can be found in Du et al. (2014). Yan and Liu (2016) use optimized pseudodifferential operators to model pure acoustic wave propagation in TTI media. Most recently, the exact factorization of the pseudoacoustic wave equation in the mixed space-wavenumber domain has been implemented using the low-rank approximation (Fomel et al., 2013; Song and Alkhalifah, 2013; Wu and Alkhalifah, 2014; Sun et al., 2016).

In this work, we derive a new pure qP-mode approximation free of physical instability and S-modes and valid even for strongly anisotropic media. Based on this new equation, we derive a separable approximation that allows for pseudospectral implementation in the mixed space-wavenumber domain. This allows us to explore its potential to provide an approximation that factors heterogeneity and anisotropy even in strongly anisotropic media in the fashion used by Liu et al. (2009) and Pestana et al. (2012) for weak anisotropy. Numerical experiments in strong anisotropic media with positive and negative anellipticity indicate the accuracy and stability of the implementation and demonstrate that the S-modes are eliminated from the proposed qP equation for weak and strong anisotropic models. We also compare the resulting wave-propagation simulations in smoothly heterogeneous media and in a more realistic model with corresponding solutions obtained with a low-rank approximation of the exact dispersion relation.

THEORY

Elastic wave propagation in a VTI medium

We start at the approximate elastic wave equation for VTI media with small δ, as specified by Bloot et al. (2013). It reads,

$$\begin{aligned}\rho\frac{\partial^2}{\partial t^2}\mathbf{u}=&\mathbf{f}+\nabla\cdot[\mu\nabla\mathbf{u}]+\nabla[(\lambda+\mu)\nabla\cdot\mathbf{u}]+\nabla\mu\times(\nabla\times\mathbf{u})+2(\nabla\mu\cdot\nabla)\mathbf{u}\\&+\hat{\nabla}[\delta(\lambda+2\mu)\nabla\cdot\mathbf{u}]+\nabla[\delta(\lambda+2\mu)\hat{\nabla}\cdot\mathbf{u}]-2\hat{\nabla}[\delta(\lambda+2\mu)\hat{\nabla}\cdot\mathbf{u}]\\&+2\hat{\nabla}^{\perp}[\mu\gamma\hat{\nabla}^{\perp}\cdot\mathbf{u}]+4\mathbf{J}\nabla\mathbf{u}\hat{\nabla}^{\perp}[\mu\gamma]+2\hat{\nabla}[\epsilon(\lambda+2\mu)\hat{\nabla}\cdot\mathbf{u}],\end{aligned}\tag{1}$$

where $\mathbf{u}=(u_1,u_2,u_3)^T$ is the displacement vector, $\mathbf{f}=(f_1,f_2,f_3)^T$ is the (external) body force, t is the time, and x_1, x_2, and x_3 denote the Cartesian coordinates. In addition, λ and μ are the Lamé parameters and ϵ, δ, and γ are the anisotropy parameters of Thomsen (1986). Moreover, the (i,j)th element of the Jacobian matrix $\nabla\mathbf{u}$ is given by $\partial u_i/\partial x_j$.

In the above equation, we use the notations,

$$\hat{\nabla}=\left(\frac{\partial}{\partial x_1},\frac{\partial}{\partial x_2},0\right)^T,\tag{2}$$

and

$$\hat{\nabla}^{\perp}=\mathbf{J}\hat{\nabla}=\left(\frac{\partial}{\partial x_2},-\frac{\partial}{\partial x_1},0\right)^T,\tag{3}$$

with

$$\mathbf{J}=\begin{pmatrix}0&1&0\\-1&0&0\\0&0&0\end{pmatrix},\tag{4}$$

as defined by Bloot et al. (2013).

Note that the derivation of equation 1 involved linearization in δ. However, it can be easily generalized to higher orders. For example, for an equation up to second order in δ, it is sufficient to replace δ by $\hat{\delta}=\delta(1-[\lambda+2\mu/\lambda+\mu]\delta)$ in equation 1.

Still according to Bloot et al. (2013), substitution of a zero-order ray ansatz (Červený, 1985, 2001) of the form,

$$\mathbf{u}(x_1,x_2,x_3,t)=\mathbf{U}(x_1,x_2,x_3)g(t-T(x_1,x_2,x_3)),\tag{5}$$

with $\mathbf{U}$ denoting a vectorial amplitude and T denoting the traveltime into the VTI wave equation without a source term yields the familiar ray-tracing eigenvalue problem:

$$\underline{\Gamma}\mathbf{U}=\mathbf{U},\tag{6}$$

where the eigenvalues must all be $\Lambda=1$. The explicit expressions for the elements of the Christoffel matrix $\underline{\Gamma}$ can be found in Bloot et al. (2013). They also show that the three eigenvalues Λ of $\underline{\Gamma}$ can be calculated exactly as

$$\Lambda_{1,2}=\frac{1}{2}\left((\alpha^2+\beta^2)\|\mathbf{p}\|^2+2\epsilon\alpha^2\|\hat{\mathbf{p}}\|^2\pm\sqrt{(\alpha^2-\beta^2)^2\|\mathbf{p}\|^4+4\Pi}\right),\tag{7}$$

where

$$\begin{aligned}\Pi=&\alpha^2[(\alpha^2-\beta^2)(\epsilon\|\mathbf{p}\|^2+2(\delta-\epsilon)p_3^2)\\&+\alpha^2(\epsilon^2\|\hat{\mathbf{p}}\|^2+\delta^2p_3^2)]\|\hat{\mathbf{p}}\|^2,\end{aligned}\tag{8}$$

and

$$\Lambda_3=\beta^2\|\mathbf{p}\|^2+2\gamma\beta^2\|\hat{\mathbf{p}}\|^2.\tag{9}$$

In these equations,

$$\mathbf{p}=\nabla T=(p_1,p_2,p_3)\ \text{ and }\ \hat{\mathbf{p}}=\hat{\nabla}T=(p_1,p_2,0)\tag{10}$$

denote the slowness vector and its horizontal projection, and

$$\alpha=\sqrt{\frac{\lambda+2\mu}{\rho}}\quad\text{and}\quad\beta=\sqrt{\frac{\mu}{\rho}}\tag{11}$$

denote the vertical P- and S-wave velocities.

Because equation 1 is already linearized in δ, we can ignore the term proportional to δ^2 in equation 8, i.e., approximate Π by

$$\Pi\approx\alpha^2[(\alpha^2-\beta^2)(\epsilon\|\mathbf{p}\|^2+2(\delta-\epsilon)p_3^2)+\alpha^2\epsilon^2\|\hat{\mathbf{p}}\|^2]\|\hat{\mathbf{p}}\|^2.\tag{12}$$

For higher order considerations, all terms in equation 8 must be taken into account.

The condition that the eigenvalues must be equal to one to represent a solution to the eigenvalue problem in equation 6 translates thus into

$$\Lambda_{1,2} = A_+ \pm \sqrt{A_-^2 - B} = 1, \tag{13}$$

and

$$\Lambda_3 = C = 1, \tag{14}$$

where

$$A_\pm = \frac{1}{2}((\alpha^2 \pm \beta^2)\|\mathbf{p}\|^2 + 2\epsilon\alpha^2\|\hat{\mathbf{p}}\|^2), \tag{15}$$

$$B = 2\alpha^2(\alpha^2 - \beta^2)(\epsilon - \delta)p_3^2\|\hat{\mathbf{p}}\|^2, \tag{16}$$

$$C = \beta^2(\|\mathbf{p}\|^2 + 2\gamma\|\hat{\mathbf{p}}\|^2). \tag{17}$$

If higher orders in δ are taken into account, equations 13 and 14 remain valid, if a term $\alpha^4 p_3^2\|\hat{\mathbf{p}}\|^2\delta^2$ is subtracted from B in equation 16.

Equation 13 with a positive sign is the qP eikonal equation that describes the kinematic properties of qP-wave propagation, and with a negative sign, it is the qSV eikonal equation. Correspondingly, equation 14 is the qSH eikonal equation. Note that equation 13 cannot be satisfied, if the argument of the square root becomes negative, which immediately implies the condition $A_-^2 \geq B$. We observe from equations 15 and 16 that this condition is virtually impossible to be violated.

Pseudoacoustic approximation

The pseudoacoustic approximation (Alkhalifah, 1998, 2000) consists of setting the vertical S-wave velocity to zero in the equations governing wave propagation. With $\beta = 0$, equations 13 and 14 become

$$\Lambda_{1,2} = a \pm \sqrt{a^2 - b} = 1, \tag{18}$$

$$\Lambda_3 = 0, \tag{19}$$

where now,

$$a = \frac{\alpha^2}{2}(\|\mathbf{p}\|^2 + 2\epsilon\|\hat{\mathbf{p}}\|^2), \tag{20}$$

$$b = 2\alpha^4(\epsilon - \delta)p_3^2\|\hat{\mathbf{p}}\|^2. \tag{21}$$

For higher orders in δ, again the term $\alpha^4 p_3^2\|\hat{\mathbf{p}}\|^2\delta^2$ must be subtracted from b in equation 21.

Equation 19 immediately implies that qSH-wave propagation is impossible in a pseudoacoustic VTI medium. At first view, the situation of qP- and qSV-wave propagation is less clear. A simple analysis of equation 18 reveals that it can be rewritten as

$$\pm\sqrt{a^2 - b} = 1 - a,\ a^2 - b = 1 - 2a + a^2,\ \text{or}\ 2a - b = 1, \tag{22}$$

i.e., with equations 20 and 21,

$$\alpha^2(\|\mathbf{p}\|^2 + 2\epsilon\|\hat{\mathbf{p}}\|^2) - 2\alpha^4(\epsilon - \delta)p_3^2\|\hat{\mathbf{p}}\|^2 = 1. \tag{23}$$

Replacing $\|\hat{\mathbf{p}}\|^2 \rightarrow (k_r^2/\omega^2)$, $p_3^2 \rightarrow (k_z^2/\omega^2)$, $\alpha^2 \rightarrow v_n^2/(1 + 2\delta)$, $(\epsilon - \delta)/(1 + 2\delta) \rightarrow \eta$, where k_r and k_z denote the horizontal and vertical wavenumbers and v_n is the normal moveout velocity, we arrive at

$$k_z^2 = \frac{v_n^2}{\alpha^2}\left(\frac{\omega^2}{v_n^2} - \frac{\omega^2 k_r^2}{\omega^2 - 2\eta v_n^2 k_r^2}\right), \tag{24}$$

which is exactly the pseudoacoustic qP dispersion relation of Alkhalifah (2000). Because in the analysis leading to equation 22, we have taken into account both signs in front of the square root, this equation is actually a dispersion relation for qP- and qSV-waves. This explains the appearance of a second arrival when modeling with equation 24. This arrival's kinematics are different from the true kinematics of the qSV-waves because the S-wave velocity is set to zero in equation 24. Below, we will analyze its behavior and the conditions for its existence.

Pseudoacoustic qP and qSV degeneration

Pseudoacoustic qP- and qSV-waves degenerate into a single arrival, if

$$\pm\sqrt{a^2 - b} = 1 - a = 0, \tag{25}$$

because then, the qP and qSV eikonal equations are identical. Equation 25 immediately implies that $a = b = 1$; i.e.,

$$a = \frac{\alpha^2}{2}((1 + 2\epsilon)\|\hat{\mathbf{p}}\|^2 + p_3^2) = 1, \tag{26}$$

$$b = 2\alpha^4(\epsilon - \delta)p_3^2\|\hat{\mathbf{p}}\|^2 = 1. \tag{27}$$

These two equations define the propagation directions in which pseudoacoustic qP- and qSV-waves travel with the same velocity. Solving equation 26 for p_3^2 and substituting the resulting expression in equation 27 results in

$$(1 + 2\epsilon)\alpha^4\|\hat{\mathbf{p}}\|^4 - 2\alpha^2\|\hat{\mathbf{p}}\|^2 + 1/(2\epsilon - 2\delta) = 0, \tag{28}$$

which can be solved for the horizontal slowness to yield

$$\|\hat{\mathbf{p}}\|^2 = \frac{1}{\alpha^2}\frac{1 \pm \sqrt{-\frac{1+2\delta}{2(\epsilon-\delta)}}}{1+2\epsilon}. \tag{29}$$

Note, however, that equations 26 and 27 cannot be satisfied simultaneously for an arbitrary VTI medium. For equation 27 to be fulfilled, we need $\epsilon - \delta > 0$. For equation 29 to represent a real propagation direction, i.e., describing a nonevanescent wave, the term under the square root must be nonnegative. This condition translates to the requirement that $\epsilon - \delta < 0$, unless $\delta = -1/2$. Thus, as already observed by Grechka et al. (2004), qP-qSV-wave degeneration is possible only in media with $\delta = -1/2$, which is actually the smallest value δ can take. Note that this is a rather large value of $|\delta|$, for which the linearized analysis is not strictly valid. The same analysis can be carried out up to second order in δ and yields $\delta = 1 - \sqrt{2} \approx -0.41$. This should be a better approximation to the true value of δ allowing for qP-qSV degeneration and demonstrates that it may occur in real media.

In a medium satisfying this condition, equation 29 reduces to

$$\alpha^2\|\hat{\mathbf{p}}\|^2 = \frac{1}{1+2\epsilon}. \tag{30}$$

The vertical slowness component is then given by substituting equation 30 into equation 26, which yields

$$\alpha^2 p_3^2 = 2 - (1+2\epsilon)\alpha^2\|\hat{\mathbf{p}}\|^2 = 1. \tag{31}$$

Equations 30 and 31 correspond to the propagation direction

$$\theta = \arctan\frac{p_1}{p_3} = \pm\arctan\frac{1}{\sqrt{1+2\epsilon}} = \pm\frac{1}{2}\arccos\frac{1}{1+\epsilon}, \tag{32}$$

as previously derived by Grechka et al. (2004).

Separate pseudoacoustic qP and qSV propagation

From the above analysis, it is clear that to propagate qP-waves or qSV-waves only, we must not rely on the common dispersion relation 24. The individual eikonal equations must be used to simulate the individual wave types, i.e.,

$$\text{qP eikonal equation: } +\sqrt{a^2 - b} = 1 - a, \tag{33}$$

$$\text{qSV eikonal equation: } -\sqrt{a^2 - b} = 1 - a. \tag{34}$$

The positive sign in front of the square root in the qP eikonal equation 33 shows that this equation can only be fulfilled if $1 - a > 0$, i.e., $a < 1$. Moreover because we are interested in describing transient waves, we need the argument of the square root to be positive, which translates into the condition $b < a^2$. Correspondingly, we see that the qSV eikonal equation 34 requires $a > 1$ and $b < a^2$. Moreover, equation 34 cannot be fulfilled if $b < 0$ because in that case the left side $-\sqrt{a^2 - b} < -a$, whereas the right side $1 - a > -a$. Thus, for transient pseudoacoustic qSV-wave propagation to be possible, we need $0 < b < a^2$. The condition $b > 0$ directly implies $\epsilon - \delta > 0$. Thus, the pseudoacoustic qSV-wave can only be observed in VTI media with $\epsilon > \delta$; i.e., $\eta > 0$.

This analysis demonstrates that the domains for qP- and qSV-waves are separated by the surface $a = 1$,

$$a = \frac{\alpha^2}{2}((1+2\epsilon)\|\hat{\mathbf{p}}\|^2 + p_3^2) = 1. \tag{35}$$

This equation describes an elliptical slowness surface with horizontal velocity $\alpha\sqrt{(1+2\epsilon)/2}$ and vertical velocity $\alpha\sqrt{1/2}$.

Approximations to the pseudoacoustic qP eikonal equation

Because we are interested in describing the propagation of qP-waves only, we need to transform equation 33 into a differential equation, which can then be solved, e.g., by means of a finite-difference approximation. However because equation 33 contains a square root, it cannot be used directly to derive an equivalent wave equation. Therefore, we study a few possible approximations to the square root.

Near-vertical propagation

The first idea is to approximate square root for near-vertical propagation, i.e., for $\|\hat{\mathbf{p}}\|^2 \ll p_3^2$. Writing the square root in equation 33 in terms of $\|\hat{\mathbf{p}}\|^2/p_3^2$, we find up to first order,

$$\begin{aligned}&\sqrt{\left(\frac{\alpha^2}{2}(\|\mathbf{p}\|^2 + 2\epsilon\|\hat{\mathbf{p}}\|^2)\right)^2 - 2\alpha^4(\epsilon-\delta)p_3^2\|\hat{\mathbf{p}}\|^2}\\ &= \frac{\alpha^2}{2}((1-2\epsilon+4\delta)\|\hat{\mathbf{p}}\|^2 + p_3^2).\end{aligned} \tag{36}$$

Substitution back in equation 33 yields an approximate elliptical eikonal equation

$$v_n^2\|\hat{\mathbf{p}}\|^2 + \alpha^2 p_3^2 = 1. \tag{37}$$

Small b approximation

Another promising idea is to approximate square root for $b \ll a^2$, given that it has to satisfy $b < a^2$ anyway for the square root to remain real. We find

$$\begin{aligned}\sqrt{a^2 - b} &= a\sqrt{1 - \frac{b}{a^2}} \approx a\left(1 - \frac{b}{2a^2}\right),\\ &= a - \frac{b}{2a}.\end{aligned} \tag{38}$$

This leads to the approximate eikonal equation:

$$a - \frac{b}{2a} \approx 1 - a, \tag{39}$$

$$\text{or} \quad 2a(2a-1) = b, \tag{40}$$

i.e.,

$$(\alpha^2\|\mathbf{p}\|^2 + 2\epsilon\|\hat{\mathbf{p}}\|^2)(\alpha^2(\|\mathbf{p}\|^2 + 2\epsilon\|\hat{\mathbf{p}}\|^2) - 1) = 2\alpha^4(\epsilon-\delta)p_3^2\|\hat{\mathbf{p}}\|^2. \tag{41}$$

The corresponding dispersion relation is

$$((1+2\eta)v_n^2k_r^2 + \alpha^2k_z^2)^2 - ((1+2\eta)v_n^2k_r^2 + \alpha^2k_z^2)\omega^2 = 2\eta v_n^2\alpha^2k_r^2k_z^2. \tag{42}$$

This equation has been previously derived from the dispersion relation 24 by Klíe and Toro (2001). These authors transformed it into a differential equation and numerically tested through an FD implementation to demonstrate its high quality for small anisotropy.

Nonacoustic qP eikonal equation

The structure of the original qP eikonal equation,

$$A_+ + \sqrt{A_-^2 - B} = 1, \tag{43}$$

is almost identical to its pseudoacoustic version 33. Therefore, the same approximation that lead to Klíe and Toro's (2001) equation above can also be directly applied to equation 43.

For $B \ll A_-^2$, we find the approximate square root,

$$\sqrt{A_-^2 - B} \approx A_- - \frac{B}{2A_-}, \tag{44}$$

which leads to the approximate eikonal equation,

$$A_+ + A_- - \frac{B}{2A_-} \approx 1, \tag{45}$$

or, with $A_+ + A_- = 2a$ (compare equations 15 and 20),

$$2A_-(2a-1) = B, \tag{46}$$

i.e.,

$$((\alpha^2-\beta^2)\|\mathbf{p}\|^2 + 2\epsilon\alpha^2\|\hat{\mathbf{p}}\|^2)(\alpha^2(\|\mathbf{p}\|^2 + 2\epsilon\|\hat{\mathbf{p}}\|^2) - 1) = 2\alpha^2(\alpha^2-\beta^2)(\epsilon-\delta)p_3^2\|\hat{\mathbf{p}}\|^2. \tag{47}$$

The corresponding dispersion relation reads,

$$([(1+2\eta)v_n^2 - \beta^2]k_r^2 + (\alpha^2-\beta^2)k_z^2)((1+2\eta)v_n^2k_r^2 + \alpha^2k_z^2 - \omega^2) = 2\eta v_n^2(\alpha^2-\beta^2)k_r^2k_z^2. \tag{48}$$

This equation has been derived in a different way by Pestana et al. (2012), based on a factorization of Alkhalifah's dispersion relation 24 by Du et al. (2008).

Equation 46 has some properties that are worthwhile to note:

- It reduces to Klíe and Toro's (2001) equation for $\beta = 0$.
- It remains stable for $\eta < 0$.
- It possesses only a weak dependence on β.

The latter observation is important because it means that the approximation can be expected to improve on Klíe and Toro's (2001) equation, if the S-wave velocity is known. To reduce the number of required parameters to the same number used in the equation of Klíe and Toro (2001), one might resort to a constant ratio between the vertical P- and S-wave velocities.

Strong-anisotropy approximation

For values of B close to A_-^2, this approximation may not have sufficient quality. A better approximation of the square root can be achieved by means of a fractional Padé approximation (Bamberger et al., 1988); i.e.,

$$A_-\sqrt{1 - \frac{B}{A_-^2}} = A_-\left(1 - \frac{q_1\frac{B}{A_-^2}}{1 - q_2\frac{B}{A_-^2}}\right), \tag{49}$$

where q_1 and q_2 are the real Padé coefficients. Their theoretical values are $q_1 = 1/2$ and $q_2 = 1/4$. The corresponding approximate eikonal equation reads,

$$A_+ + A_- - \frac{q_1\frac{B}{A_-}}{1 - q_2\frac{B}{A_-^2}} = 1, \tag{50}$$

or, equivalently,

$$(A_-^2 - q_2B)(2a-1) = q_1A_-B. \tag{51}$$

Explicitly, it becomes

$$\begin{aligned}&[((\alpha^2-\beta^2)\|\mathbf{p}\|^2 + 2\epsilon\alpha^2\|\hat{\mathbf{p}}\|^2)^2 - 8q_2\alpha^2(\alpha^2-\beta^2)\\ &\times(\epsilon-\delta)p_3^2\|\hat{\mathbf{p}}\|^2](\alpha^2(\|\mathbf{p}\|^2 + 2\epsilon\|\hat{\mathbf{p}}\|^2) - 1)\\ &= 4q_1((\alpha^2-\beta^2)\|\mathbf{p}\|^2 + 2\epsilon\alpha^2\|\hat{\mathbf{p}}\|^2)\alpha^2(\alpha^2-\beta^2)(\epsilon-\delta)p_3^2\|\hat{\mathbf{p}}\|^2,\end{aligned} \tag{52}$$

which yields the dispersion relation:

$$\begin{aligned}&[([(1+2\eta)v_n^2 - \beta^2]k_r^2 + (\alpha^2-\beta^2)k_z^2)^2 - 8q_2\eta v_n^2\\ &\times(\alpha^2-\beta^2)k_r^2k_z^2](((1+2\eta)v_n^2k_r^2 + \alpha^2k_z^2 - \omega^2)\\ &= 4q_1([(1+2\eta)v_n^2 - \beta^2]k_r^2 + (\alpha^2-\beta^2)k_z^2)\eta v_n^2\\ &\times(\alpha^2-\beta^2)k_r^2k_z^2.\end{aligned} \tag{53}$$

We will see below that this approximation is highly accurate even for strong anisotropy.

Separable approximations

The problem with the above approximations is that they are unsuitable for efficient wave-propagation simulation in the time-wavenumber domain in heterogeneous media. A feasible way to

solve them is using low-rank approximations, which can be very demanding on storage and computational cost for strongly heterogeneous media. In this sense, they provide no advantage over the full qP eikonal equation 43 involving a square root, which can also be solved using a low-rank approximation. For an efficient implementation in the spectral domain, a separable approximation is required. The computational cost of separable approximations does not depend on the medium heterogeneity.

Linear approximation

For this reason, Pestana et al. (2012) introduce an additional approximation to their version of the dispersion relation. They express their approximation of the dispersion relation (here obtained from the linear approximation of the square root) as

$$\omega^2 = (1+2\eta)v_n^2 k_r^2 + \alpha^2 k_z^2 - \frac{2\eta v_n^2 k_r^2 k_z^2}{k_z^2 + F k_r^2}, \tag{54}$$

where they use the notations

$$F = \frac{(1+2\eta)v_n^2 - \beta^2}{\alpha^2 - \beta^2} = 1 + \frac{2\epsilon}{f}, \text{and } f = 1 - \frac{\beta^2}{\alpha^2}. \tag{55}$$

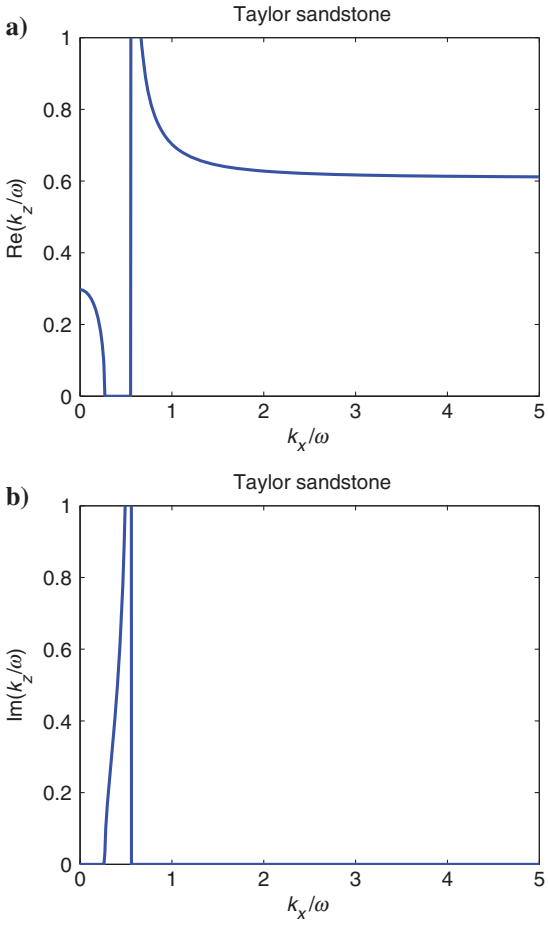

Figure 1. Pseudoacoustic qP dispersion relation for Taylor sandstone: (a) real part and (b) imaginary part. The dispersion relation becomes imaginary at the horizontal P-wave velocity, but turns real again for larger k_r.

The separable approximation proposed by Pestana et al. (2012) is to use $F \approx 1$, which eliminates the S-wave velocity from the approximation. We note, however, that this is a stronger assumption than the pseudoacoustic approximation, which sets $\beta = 0$.

Second-order approximation

The corresponding version of the strong-anisotropy approximation 53 reads,

$$\omega^2 = (1+2\eta)v_n^2 k_r^2 + \alpha^2 k_z^2 - 2q_1 \frac{2\eta v_n^2 k_r^2 k_z^2}{k_z^2 + F k_r^2 - 4q_2 G}, \tag{56}$$

where

$$G = \frac{2(\epsilon - \delta)}{f} \frac{k_r^2 k_z^2}{k_z^2 + F k_r^2}. \tag{57}$$

For $q_1 = 1/2$ and $q_2 = 0$, it reduces to equation 54.

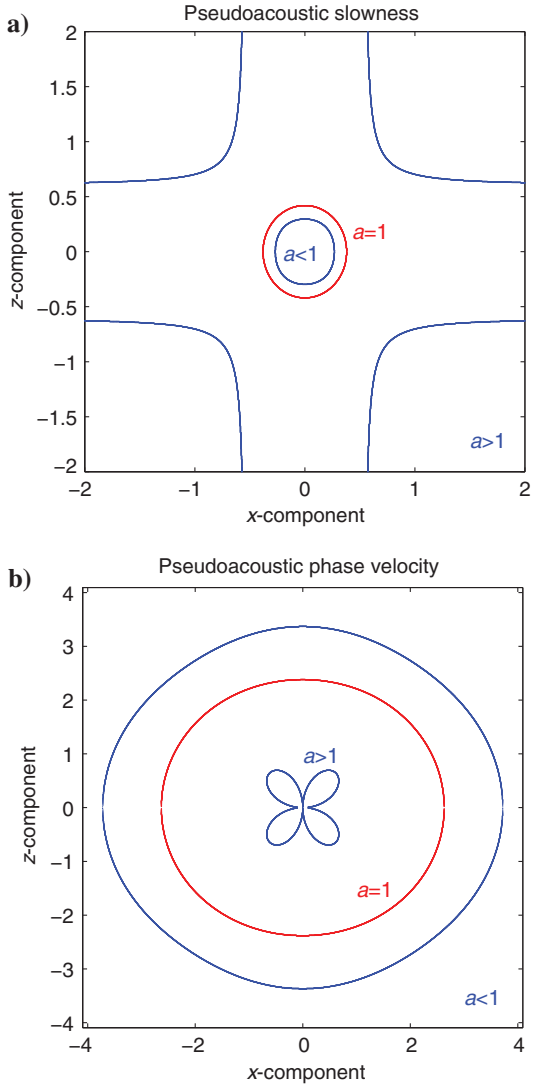

Figure 2. (a) Slowness and (b) phase-velocity surfaces for Taylor sandstone. The domains for qP and qSV propagation are separated by the surface $a = 1$ (red line).

To obtain a separable approximation that remains valid for strong anisotropy, we first put $k^2 = k_r^2 + k_z^2$ into evidence in the denominator of equation 56 and then approximate the resulting expression up to first order in the anisotropy parameters. In symbols,

$$\omega^2 = (1+2\eta)v_n^2k_r^2+\alpha^2k_z^2-2q_1\frac{2\eta v_n^2k_r^2k_z^2}{k^2\left(1+\frac{2\epsilon}{f}\frac{k_r^2}{k^2}-\frac{4q_2G}{k^2}\right)},$$
$$= (1+2\eta)v_n^2k_r^2+\alpha^2k_z^2-2q_1 \times\frac{2\eta v_n^2k_r^2k_z^2}{k^2}\left(1-\frac{2\epsilon}{f}\frac{k_r^2}{k^2}-\frac{4q_2G}{k^2}\right). \quad (58)$$

Then, we approximate G correspondingly; i.e.,

$$G = \frac{2(\epsilon-\delta)}{f}\frac{k_r^2k_z^2}{k^2\left(1+\frac{2\epsilon}{f}\frac{k_r^2}{k^2}\right)},$$
$$= \frac{2(\epsilon-\delta)}{f}\frac{k_r^2k_z^2}{k^2}\left(1-\frac{2\epsilon}{f}\frac{k_r^2}{k^2}\right). \quad (59)$$

Substitution of equation 59 in equation 58 yields, up to third order in $1/k^2$,

$$\omega^2 = (1+2\eta)v_n^2k_r^2+\alpha^2k_z^2-2q_1\frac{2\eta v_n^2k_r^2k_z^2}{k^2} \times\left(1-\frac{2\epsilon}{f}\frac{k_r^2}{k^2}-\frac{8q_2(\epsilon-\delta)}{f}\frac{k_r^2k_z^2}{k^4}\right). \quad (60)$$

Table 1. Materials used for the analysis of the approximations to the dispersion relation.

Material	α (km/s)	β (km/s)	ϵ	δ	η
Mesaverde mudshale	4.529	2.703	0.034	0.211	−0.124
Taylor sandstone	3.368	1.829	0.110	−0.035	0.156
Mesaverde laminated siltstone	4.449	2.585	0.091	0.565	−0.223
Shale TH-51, sample 13	3.431	2.020	0.550	0.070	0.421
Dry Green River shale	3.292	1.768	0.195	−0.220	0.741
Biotite crystal	4.054	1.341	1.222	−0.388	7.1875

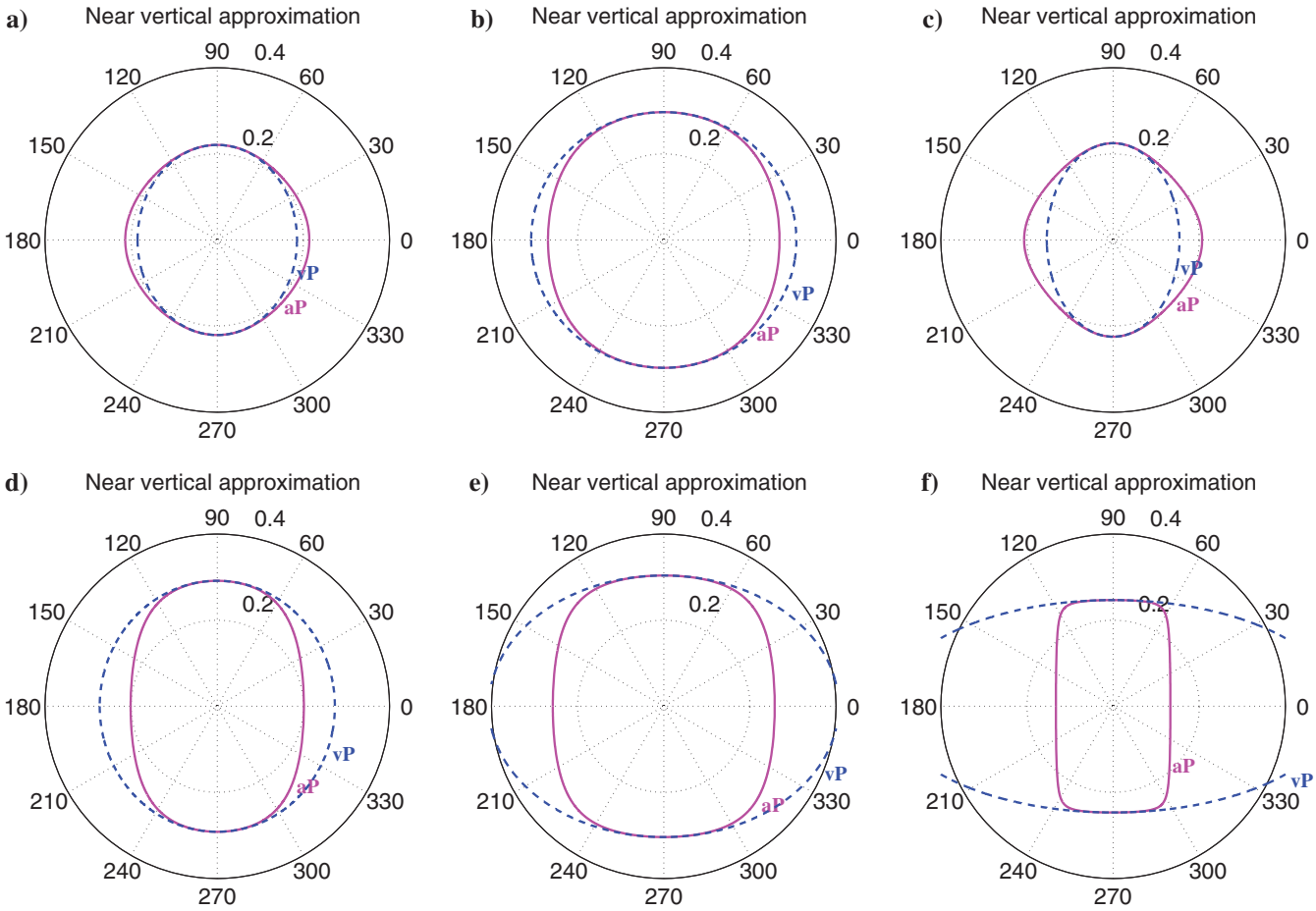

Figure 3. Pseudoacoustic slowness surface (magenta line) and its near-vertical approximation (dashed blue line) for (a) Mesaverde mudshale, (b) Taylor sandstone, (c) Mesaverde laminated siltstone, (d) Shale TH-51/13, (e) dry Green River shale, and (f) biotite crystal.

Alternatively, we can use $f = 1 - \beta^2/\alpha^2$ and assume that the velocity ratio is also small. This yields

$$\omega^2 = (1+2\eta)v_n^2 k_r^2 + \alpha^2 k_z^2 - 2q_1 \frac{2\eta f v_n^2 k_r^2 k_z^2}{k^2\left(1 - \frac{\beta^2}{\alpha^2} + \frac{2\epsilon k_r^2}{k^2} - \frac{4fq_2 G}{k^2}\right)},$$
$$= (1+2\eta)v_n^2 k_r^2 + \alpha^2 k_z^2 - 2q_1 \times \frac{2\eta f v_n^2 k_r^2 k_z^2}{k^2}\left(1 + \frac{\beta^2}{\alpha^2} - \frac{2\epsilon k_r^2}{k^2} - \frac{4q_2 f G}{k^2}\right). \quad (61)$$

The corresponding approximation of G reads

$$G = \frac{2(\epsilon-\delta)k_r^2 k_z^2}{fk^2 + 2\epsilon k_r^2} = \frac{2(\epsilon-\delta)k_r^2 k_z^2}{k^2\left(1 - \frac{\beta^2}{\alpha^2} + \frac{2\epsilon k_r^2}{k^2}\right)},$$
$$= \frac{2(\epsilon-\delta)k_r^2 k_z^2}{k^2}\left(1 + \frac{\beta^2}{\alpha^2} - \frac{2\epsilon k_r^2}{k^2}\right). \quad (62)$$

Substitution of equation 62 in equation 61 yields, up to third order in $1/k^2$:

$$\omega^2 = (1+2\eta)v_n^2 k_r^2 + \alpha^2 k_z^2 - 2q_1 \frac{2\eta v_n^2 k_r^2 k_z^2}{k^2} \times \left[1 - \frac{\beta^4}{\alpha^4} - \frac{2\epsilon f k_r^2}{k^2} - \frac{8q_2 f(\epsilon-\delta)k_r^2 k_z^2}{k^4}\left(1 - \frac{\beta^4}{\alpha^4}\right)\right], \quad (63)$$

or, also neglecting β^4/α^4 to be consistent with the above approximations:

$$\omega^2 = (1+2\eta)v_n^2 k_r^2 + \alpha^2 k_z^2 - 2q_1 \frac{2\eta v_n^2 k_r^2 k_z^2}{k^2} \times \left[1 - \frac{2\epsilon f k_r^2}{k^2} - \frac{8q_2 f(\epsilon-\delta)k_r^2 k_z^2}{k^4}\right]. \quad (64)$$

In effect, equations 60 and 64 can be represented as

$$\omega^2 = (1+2\eta)v_n^2 k_r^2 + \alpha^2 k_z^2 - 2q_1 \frac{2\eta v_n^2 k_r^2 k_z^2}{gk^2} \times \left[g - \frac{2\epsilon k_r^2}{k^2} - \frac{8q_2(\epsilon-\delta)k_r^2 k_z^2}{k^4}\right], \quad (65)$$

with three possible choices for g, being

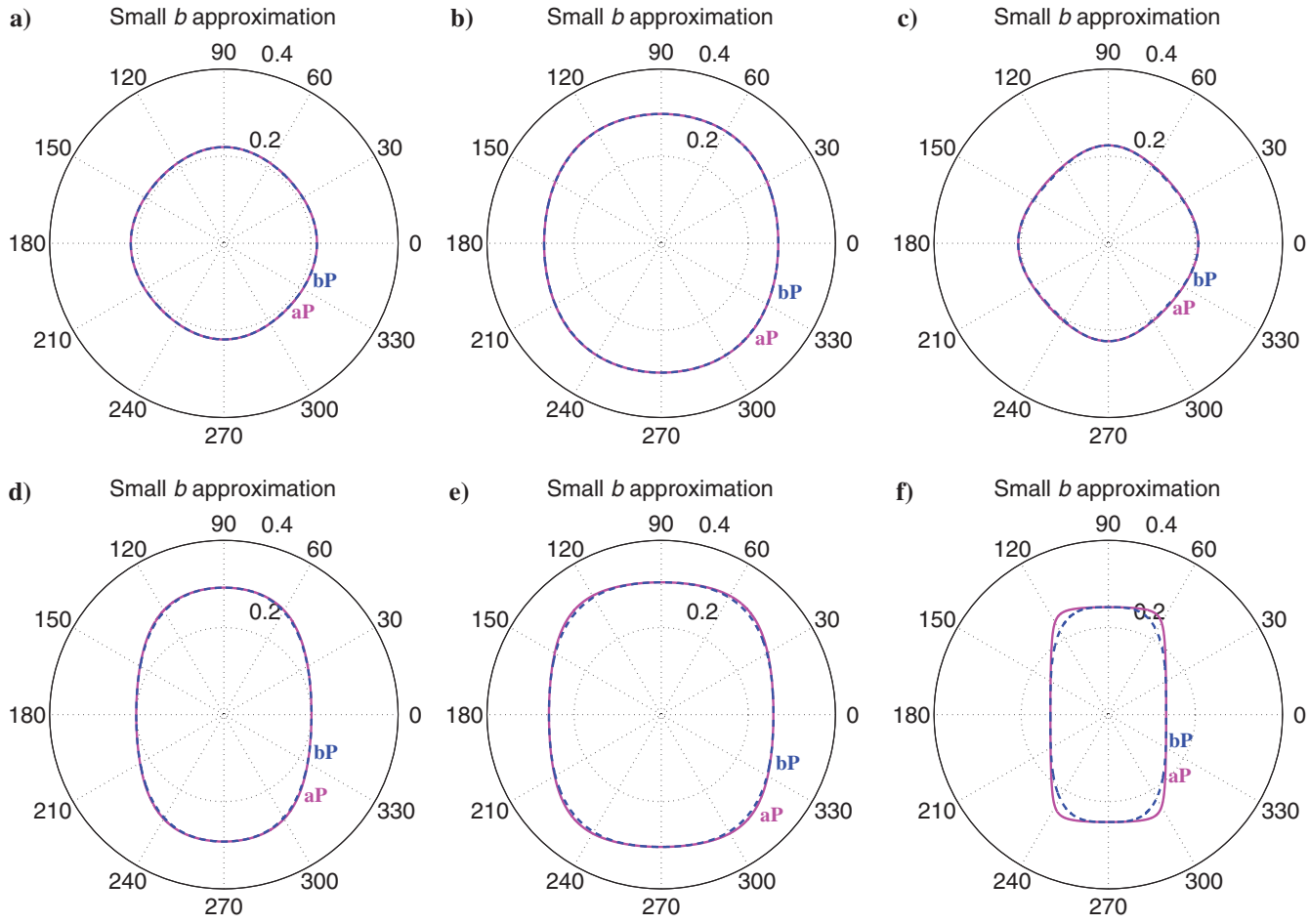

Figure 4. Pseudoacoustic slowness surface (magenta line) and its small b approximation (dashed blue line) for (a) Mesaverde mudshale, (b) Taylor sandstone, (c) Mesaverde laminated siltstone, (d) Shale TH-51/13, (e) dry Green River shale, and (f) biotite crystal.

$$g = f \quad \text{or} \quad g = \frac{1}{f} \quad \text{or} \quad g = 1. \tag{66}$$

The latter choice of $g = 1$ is obtained from setting $\beta = 0$. In other words, it represents the pseudoacoustic version of this equation. This choice reduces the number of parameters describing the wave propagation to the same number used in the previous approximations. Our numerical experiments indicate that the influence of this term is rather small, so that the choice $g = 1$ should be sufficient in most cases.

Equation 65 can be conveniently implemented in the mixed space-wavenumber domain by calculating the involved derivatives in the wavenumber domain and then applying space-variable scaling in the space domain. Because the derivative calculations can be carried out with respect to local coordinates for each point in the model space, equation 65 can be immediately used for an implementation in TTI media in a similar way to the ones indicated by Zhan et al. (2013) or Zhou et al. (2015).

For comparison, we have implemented a low-rank solution (Fomel et al., 2013) to the dispersion relation of the original qP-wave eikonal equation 43. We computed the low-rank approximation matrix using the algebraic reconstruction technique according to Kaczmarz (1993). The low-rank approximation permits approximation of an arbitrary dispersion relation with any desired precision. It requires a prediction of the rank of the approximation of matrix. In the examples in this work, we always used the smallest number that kept the residual below a specified level. Note that the required rank depends on the medium heterogeneity and anisotropy.

NUMERICAL EXAMPLES

To better understand the S-wave mode in the pseudoacoustic approximation and to demonstrate the quality of the approximations obtained from the above analysis, we have calculated a few slowness surfaces and modeled wave propagation for a set of materials with different anisotropies.

Pseudoacoustic qP dispersion relation

The S-wave modes in the pseudoacoustic approximation are best understood from an analysis of the pseudoacoustic qP dispersion relation. Figure 1 shows this relation for the parameters of Taylor sandstone (Thomsen, 1986): $\alpha = 3.368$ km/s, $\beta = 1.829$ km/s, $\epsilon = 0.110$, $\delta = -0.035$, i.e., $\eta = 0.156 > 0$ for this material.

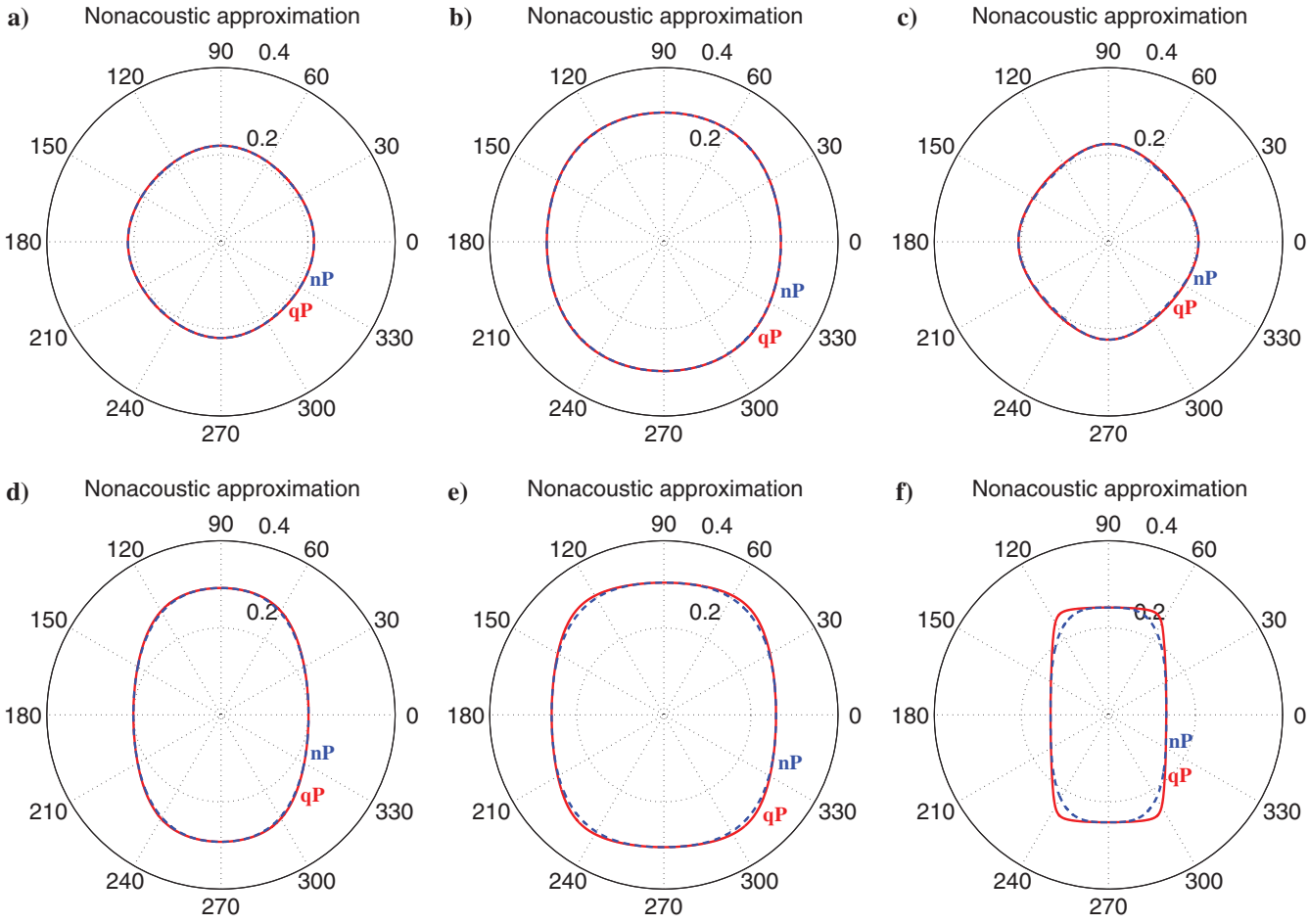

Figure 5. True qP slowness surface (red line) and its nonacoustic approximation (dashed blue line) for (a) Mesaverde mudshale, (b) Taylor sandstone, (c) Mesaverde laminated siltstone, (d) shale TH-51/13, (e) dry Green River shale, and (f) biotite crystal.

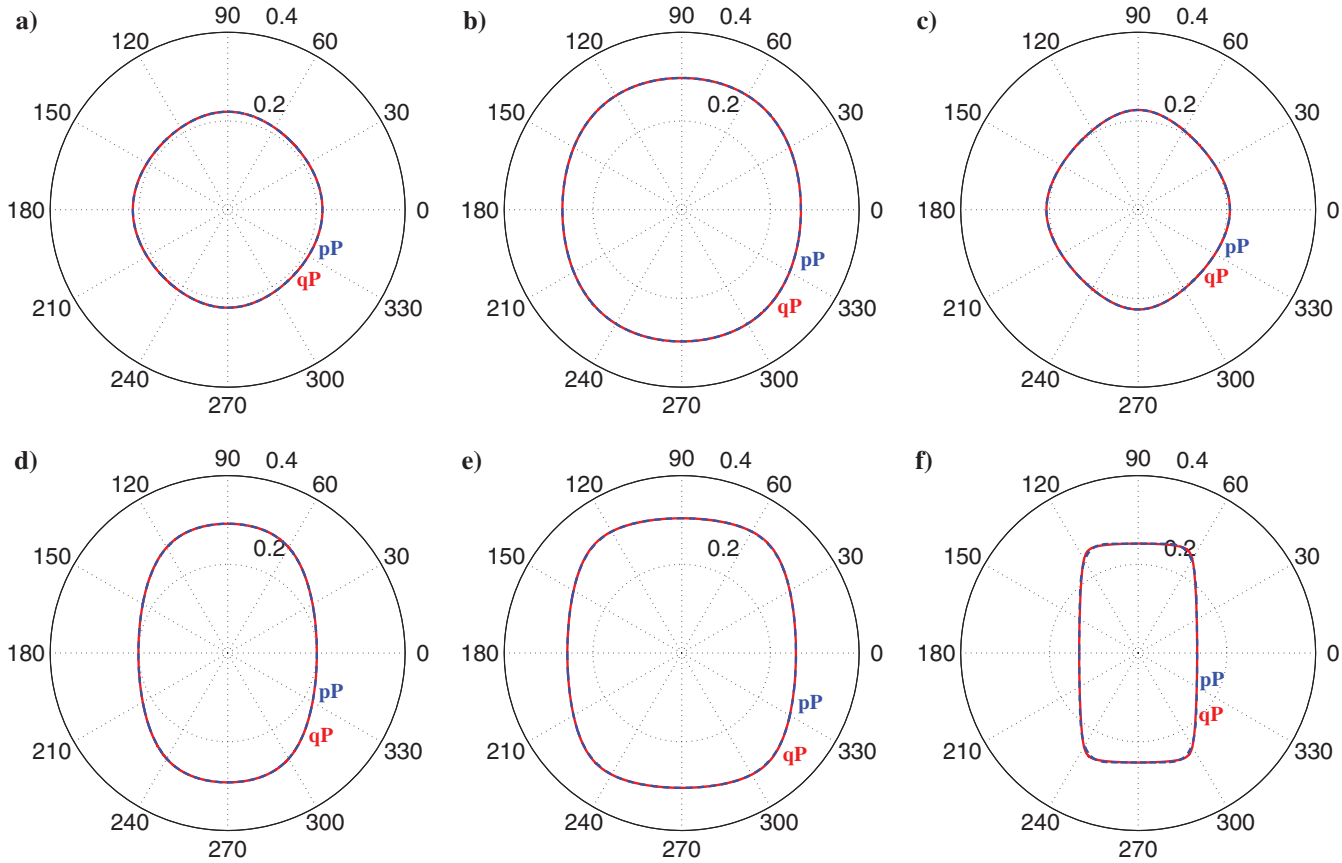

Figure 6. True qP slowness surface (red line) and its nonacoustic Padé approximation with anisotropy-dependent coefficients (dashed blue line) for (a) Mesaverde mudshale, (b) Taylor sandstone, (c) Mesaverde laminated siltstone, (d) shale TH-51/13, (e) dry Green River shale, and (f) biotite crystal.

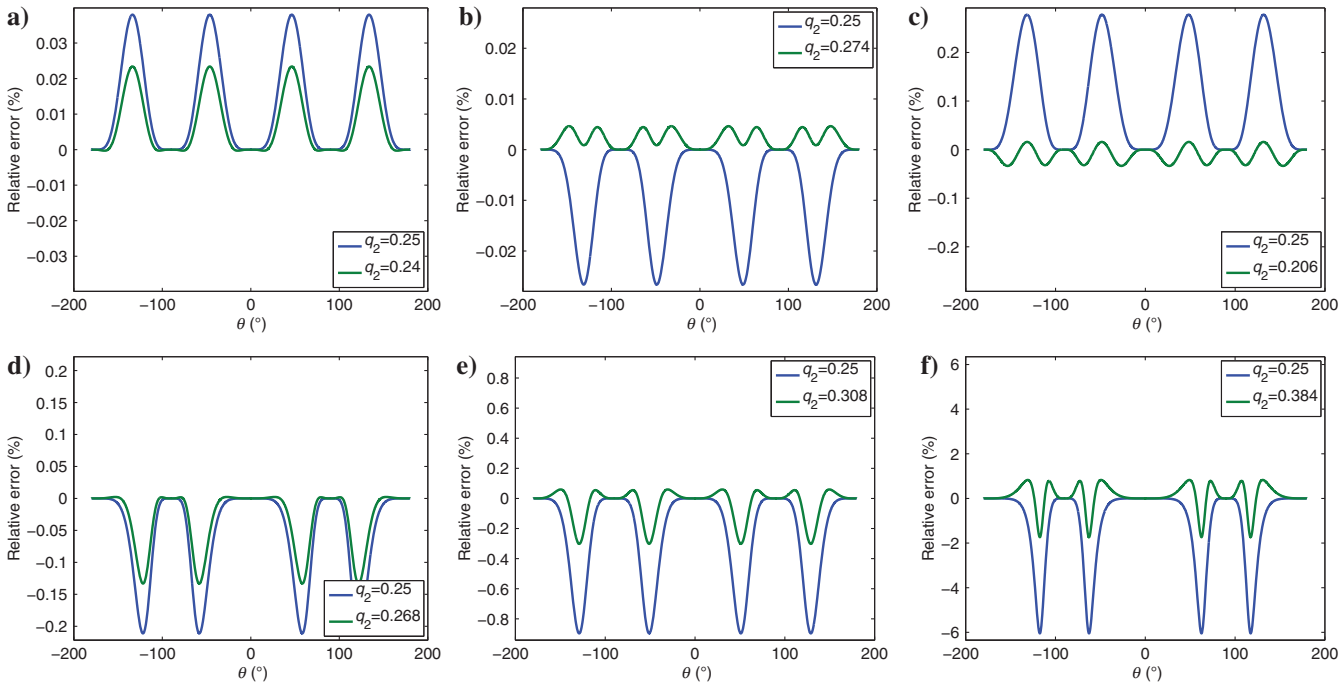

Figure 7. Error of nonacoustic slowness surface for theoretical (blue line) and anisotropy-dependent value of q_2 (green line) for (a) Mesaverde mudshale, (b) Taylor sandstone, (c) Mesaverde laminated siltstone, (d) shale TH-51/13, (e) dry Green River Shale, and (f) biotite crystal.

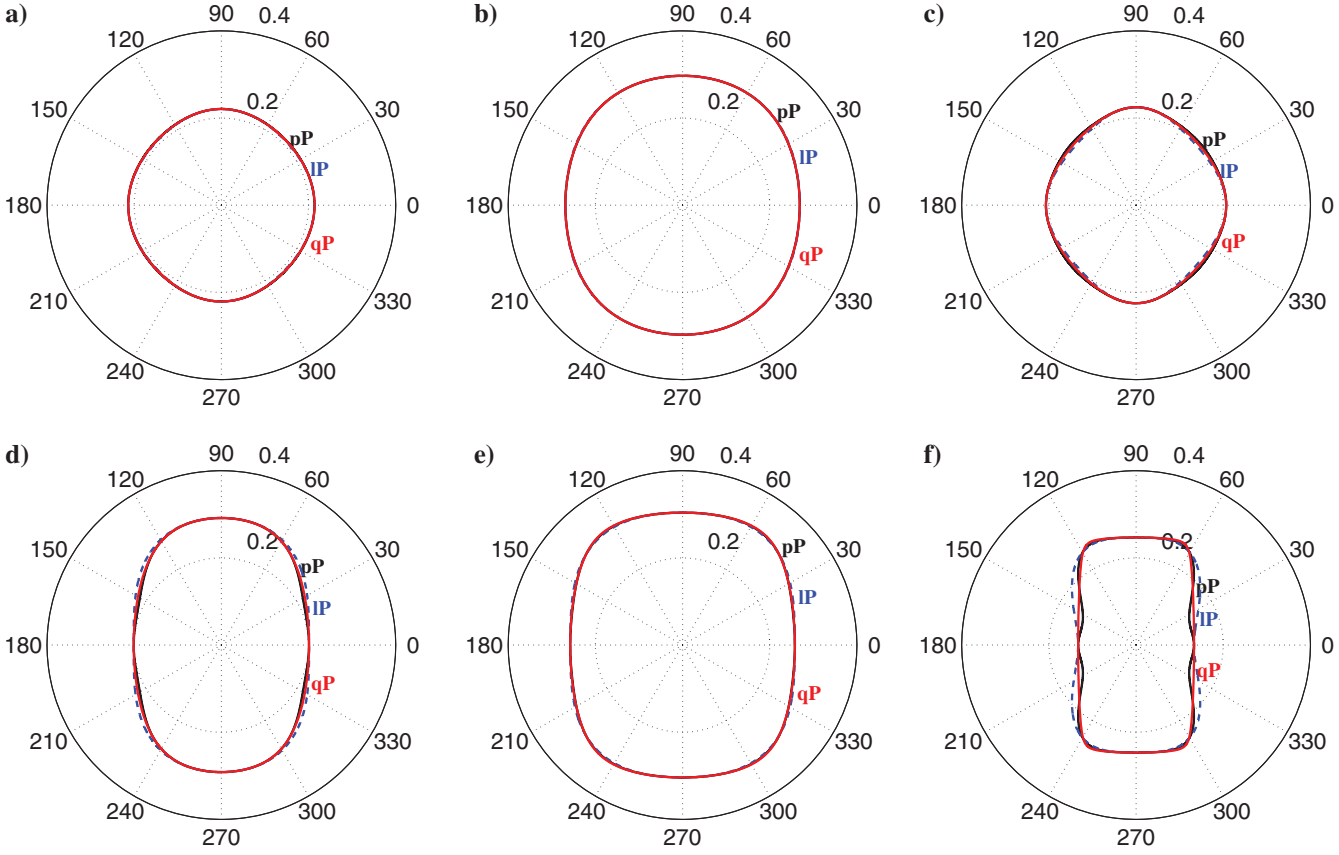

Figure 8. True qP slowness surface (red line) and its separable nonacoustic Padé approximation (dashed blue line) for (a) Mesaverde mudshale, (b) Taylor sandstone, (c) Mesaverde laminated siltstone, (d) shale TH-51/13, (e) dry Green River shale, and (f) biotite crystal.

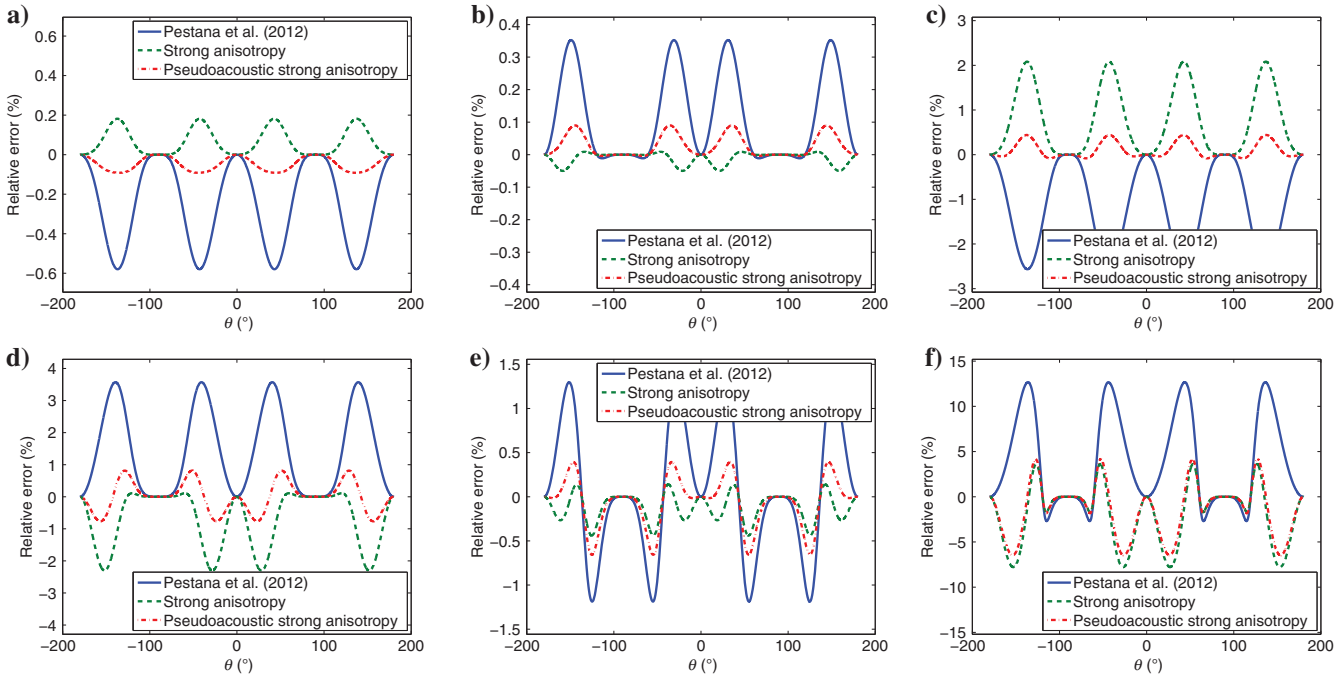

Figure 9. Error of pseudoacoustic slowness surface for linear (solid blue line) and separable full (dashed green line) and pseudoacoustic (dash-dotted red line) strong-velocity approximations for (a) Mesaverde mudshale, (b) Taylor sandstone, (c) Mesaverde laminated siltstone, (d) shale TH-51/13, (e) dry Green River shale, and (f) biotite crystal.

We observe in Figure 1 that the dispersion relation becomes imaginary at the horizontal P-wave velocity, but turns real again for larger k_r (Amazonas et al., 2010). These larger wavenumbers correspond to a slower wave propagation, as shown in Figure 2. Also shown in this figure is the surface $a = 1$ (red curve), which separates the domains for qP- and qSV-wave propagations. In Figure 2a, these slower wave components are outside the red curve (larger slowness), whereas in Figure 2b, they appear inside (smaller phase velocity).

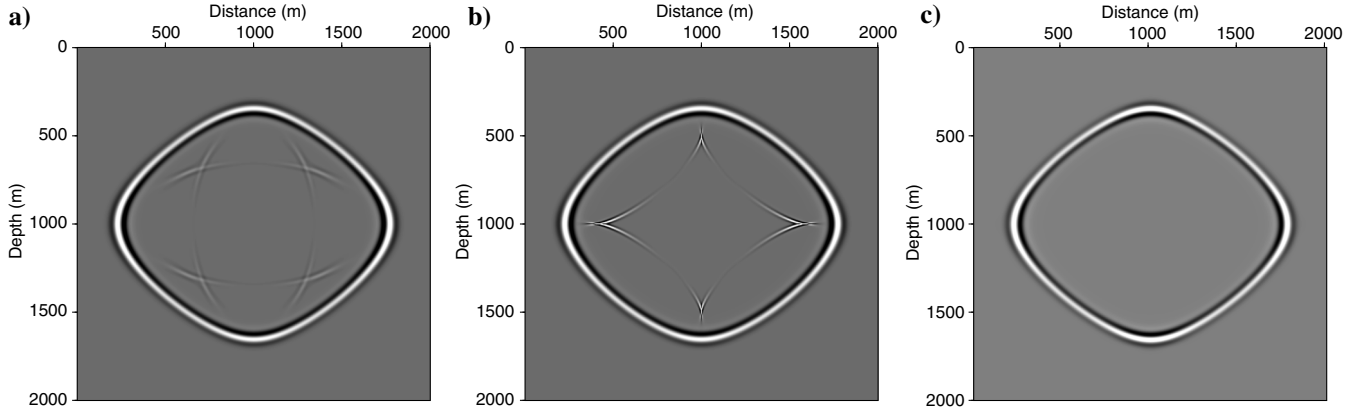

Figure 10. Snapshots at $t = 212$ ms of qP-wave in a homogeneous dry Green River Shale. (a) Full-tension wavefield. (b) Pseudoacoustic wavefield. (c) Nonacoustic strong-anisotropy approximation.

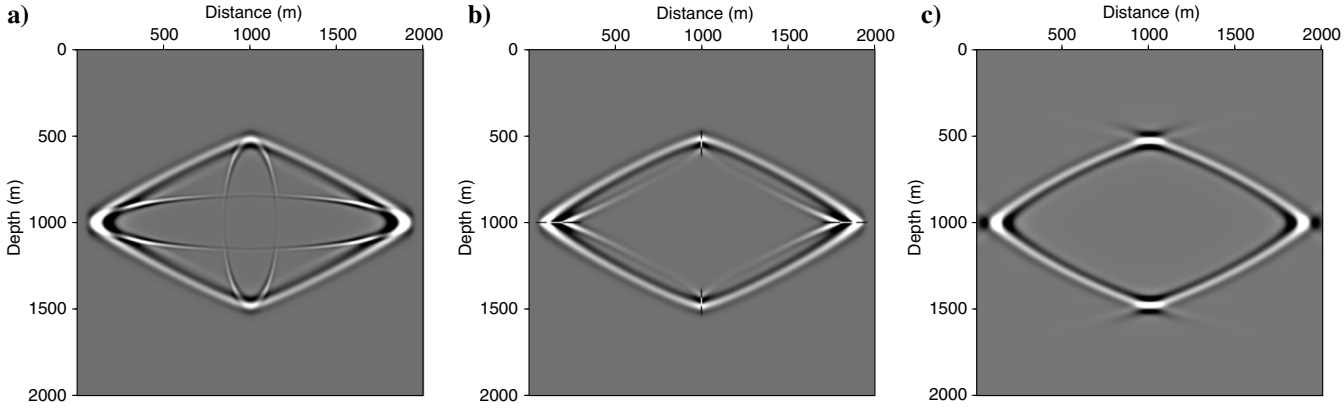

Figure 11. Snapshots at $t = 140$ ms of qP-wave in a homogeneous biotite crystal. (a) Full-tension wavefield. (b) Pseudoacoustic wavefield. (c) Nonacoustic strong-anisotropy approximation.

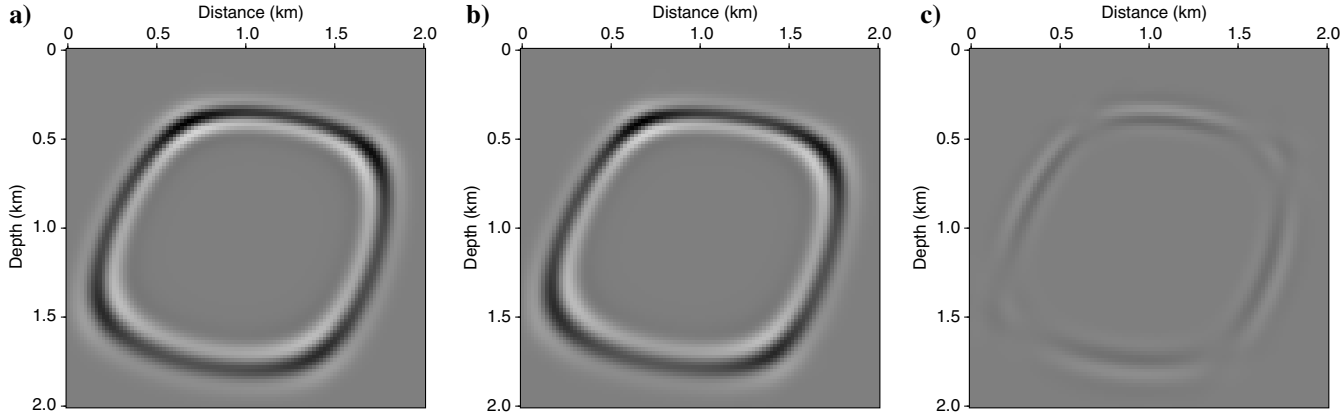

Figure 12. Snapshots at $t = 212$ ms of qP-wave in an inhomogeneous anisotropic TTI model. (a) True qP wavefield. (b) Nonacoustic strong-anisotropy approximation. (c) Difference of normalized wavefields.

qP relation for near-vertical propagation

Our first approximation for the pure qP dispersion relation is equation 37 for near-vertical propagation. Figure 3 shows this approximation for six different materials with very different anisotropic properties. These materials are Mesaverde mudshale, Taylor sandstone, Mesaverde laminated siltstone, dry Green River shale, and biotite crystal (Thomsen, 1986) as well as shale TH-51, sample 13 (Johnston and Christensen, 1995). Their anisotropic parameters are listed in Table 1. In Figure 3, the approximation correctly describes the slowness surface for propagation directions up to approximately 25°–30° for all tested materials, including the extremely anisotropic Biotite Crystal.

Small *b* approximation

Better approximation is achieved for all of these materials with the small b approximation of equation 40, previously derived by Klíe and Toro (2001). A comparison with the true pseudoacoustic slowness surface for the four cited materials is shown in Figure 4. We see that for Mesaverde mudshale, Taylor sandstone, Mesaverde laminated siltstone, and shale TH-51/13 (Figure 4a–4d), the small b approximation is virtually indistinguishable from the pseudoacoustic slowness surface. Even for the rather strongly anisotropic dry Green River shale (Figure 4e), the differences are quite small and occur almost exclusively in the diagonal directions. Only for the extremely anisotropic biotite crystal (Figure 4f), significant differences are visible.

Nonacoustic approximations

Then, we analyze the quality of the nonacoustic approximations of equations 46 and 51. Figure 5 compares the approximation of equation 46, previously derived by Pestana et al. (2012), with the true qP slowness surface. The quality of the approximation is practically identical to that achieved by equation 40 of Klíe and Toro (2001) with respect to the pseudoacoustic slowness surface.

Figure 6 demonstrates the improved quality of the strong-anisotropy approximation. The approximated slowness surfaces are virtually identical to the true ones. Even for the biotite crystal (Figure 6f), no deviation between the true and approximated slowness surfaces is visible. Here, we used the theoretical value of $q_1 = 1/2$ for the first Padé coefficient, but chose the second one q_2 to be represented in dependence on ϵ and δ according to the function $q_2 = 1/(3.75 + 2\epsilon - 3\delta/10)$ instead of the theoretical value $q_2 = 1/4$. We found this function by means of a least-squares fit, adjusting $1/q_2$ as a linear function of ϵ and δ to the numerical values, which minimized the phase error for each of the tested model samples.

Figure 7 shows the relative error of the slowness as a function of the propagation angle in the chosen materials for the theoretical and

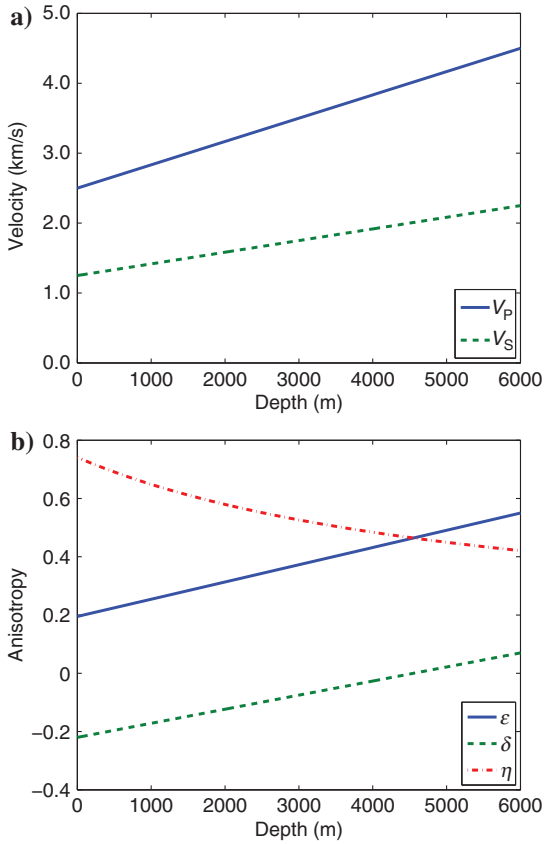

Figure 13. Model parameters of heterogeneous TTI model with constant tilt axis of 30°. (a) Vertical velocities. (b) Anisotropy parameters.

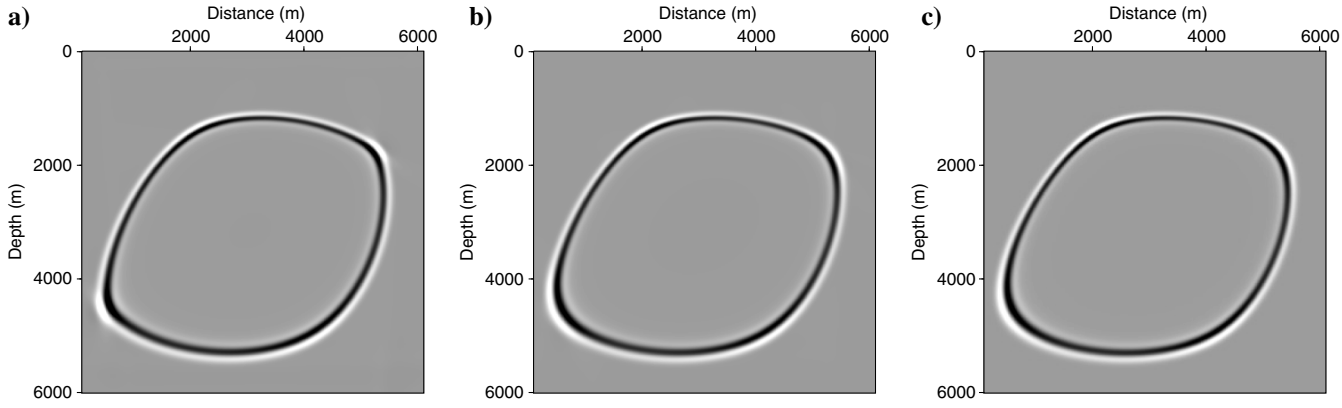

Figure 14. Snapshots at $t = 212$ ms of qP-wave in a heterogeneous TTI model with constant tilt of 30°. (a) Linear separable approximation. (b) Strong-anisotropy separable approximation. (c) Low-rank approximation.

anisotropy-dependent value of the second Padé coefficient q_2. We see that the error is visibly reduced when using the latter.

Separable approximations

Finally, we evaluate the quality of the separable approximations. Figure 8 compares the quality achieved by our strong-anisotropy approximation in equation 60 and the linear approximation of Pestana et al. (2012) in equation 54.

Figure 9 shows the relative error of the slowness in the nonacoustic separable approximations as a function of the propagation angle for the chosen materials. We see that the strong-anisotropy approximation reduces the error by approximately 50% even for the materials with smaller anisotropy. The largest reduction is achieved for Taylor sandstone (Figure 9b), whereas the least reduction occurs for Mesaverde laminated siltstone (Figure 9c).

Figure 9 also shows the relative error of the slowness in the pseudoacoustic versions ($g = 1$ in equation 60) of the separable approximations as a function of the propagation angle for the chosen materials. We see that the strong-anisotropy approximation has about the same quality as before, indicating that there is no need for the use of the S-wave velocity as an additional parameter.

Propagation snapshots

Encouraged by these very good approximations of the slowness surface, we implemented schemes to simulate numerical wave propagation by means of these equations. The first implementation was a low-rank approximation to the strong-anisotropy approximation of equation 53. Figure 10 compares snapshots in a homogeneous dry Green River Shale and Figure 11 in biotite crystal. Figures 10a and 11a show the true wavefield with qP- and qSV-waves, Figures 10b and 11b show the pseudoacoustic wavefield with the approximate qP-wave and an incorrect qSV-wave, and Figures 10c and 11c show the nonacoustic Padé approximation to the pure qP-wave. We recognize that even for these media with very strong anisotropy, the nonacoustic Padé approximation provides a very good approximation of the qP wavefront, while eliminating the S-mode entirely. In Figure 11, we see small artifacts at the most strongly curved parts of the wavefront. They appear because of the extreme anisotropy of biotite crystal, which causes our approximation to become slightly nonconvex. We note, however, that these artifacts did not cause instabilities in the propagation simulations.

Inhomogeneous media

Heterogeneous velocity, homogeneous anisotropy, and constant tilt

Our next test simulated qP-wave propagation in an inhomogeneous anisotropic TTI medium with vertical constant gradient in α from 2.5 km/s at the top of the model to 4.5 m/s at the bottom. The transformation of the above VTI equations to TTI follows the one of Zhan et al. (2013), but we calculate the spatial derivatives

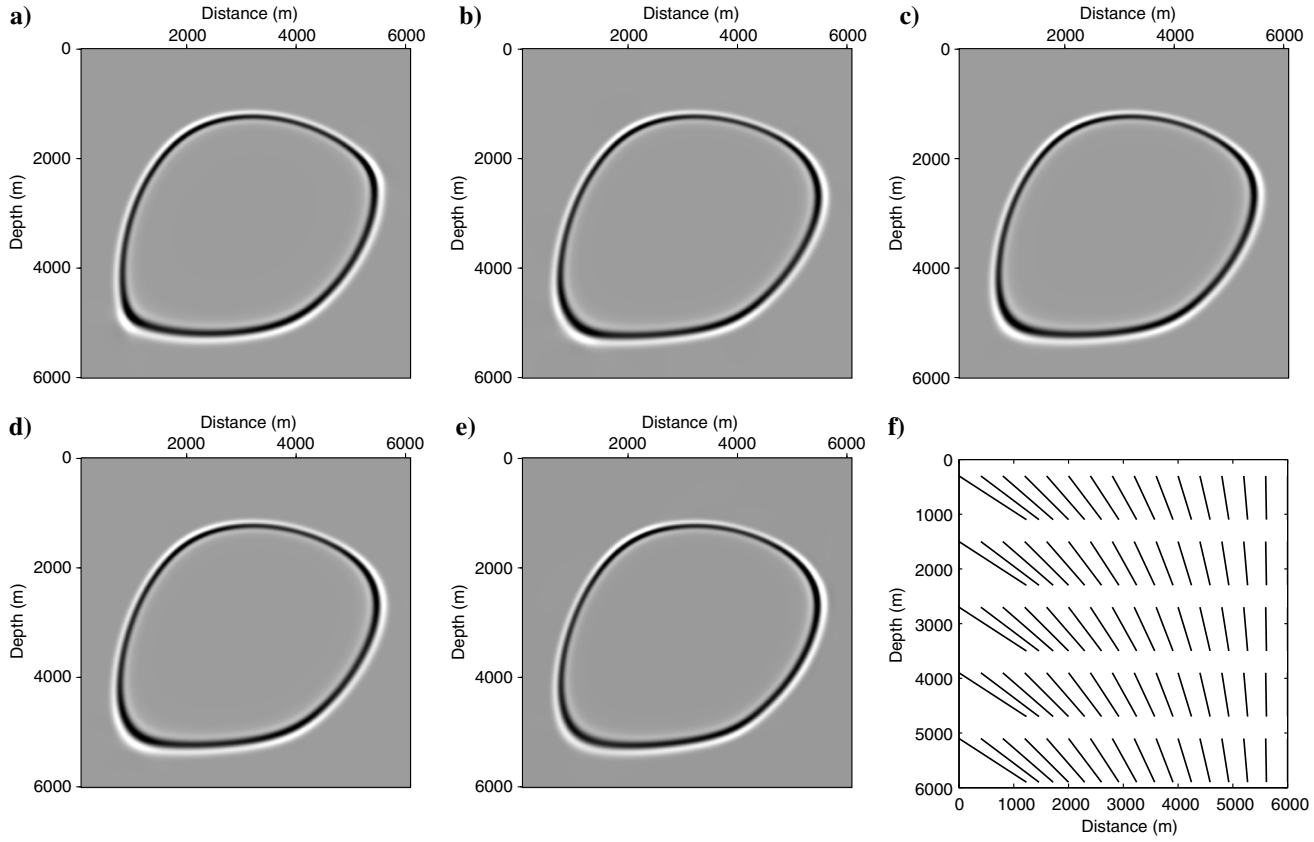

Figure 15. Snapshots at $t = 212$ ms of qP-wave in a heterogeneous TTI model with variable tilt. Comparison of separable with low-rank approximation. (a) Linear. (b) Strong anisotropy, $g = 1/f$. (c) Strong anisotropy, $g = f$. (d) Strong anisotropy, $g = 1$. (e) Low-rank approximation. (f) Tilt variation in the model.

completely in the pseudospectral domain. The anisotropy parameters are homogeneous with values $\epsilon = 0.195$ and $\delta = -0.220$ (taken from the dry Green River Shale), and the symmetry axis is tilted by a constant angle of 30° from the vertical. Figure 12 compares the result of low-rank approximate modeling of the original qP dispersion relation (Figure 12a) with the result of approximate equation 51 (Figure 12b). Even for this rather strong anisotropy and velocity gradient, we observe almost perfect coincidence between the true and approximated wavefields.

Figure 12c shows the difference between the normalized wavefields so as to show the major differences between the methods. We note that even after normalization, the most important differences are due to amplitude variations. The amplitudes of the approximate wavefield are less uniform than the true ones. Therefore, in the directions of wavefield focussing, where the highest amplitudes are located, the differences after normalization are almost zero. In the other directions, the approximate wavefield has relatively lower amplitude, resulting in a more visible difference wavefield. Because of the dominance of amplitude effects, possible phase differences are hard to detect.

Separable approximation

The final numerical tests evaluate the separable approximations 54 and 60, which we implemented in the mixed space-wavenumber domain, and compare them with a low-rank approximation of the original equation 13.

Heterogeneous anisotropy parameters, constant tilt

For the first test of the separable approximations, we used an inhomogeneous model, in which the velocity and the anisotropy parameters are heterogeneous (see parameters in Figure 13).

Figure 14 compares the modeling results with the linear separable approximation (Figure 14a) with the ones with the strong-anisotropy separable approximation (Figure 14b) and the low-rank approximation (Figure 14c).

Heterogeneous anisotropy parameters, varying tilt

Our next test used the same model parameters as the previous one, with the TI symmetry axis now varying from 0° to 60°. Figure 15 shows the varying tilt and compares the modeling results with the linear separable approximation (Figure 15a) to the ones with the strong-anisotropy separable approximation using $g = f$ (Figure 15b), $g = 1/f$ (Figure 15c), and $g = 1$ (Figure 15d), and the low-rank approximation of the square-root equation (Figure 15e). We see that the second-order approximations resemble the low-rank result more closely than the first-order approximation. Between the second-order approximations, the differences are rather subtle. Closer inspection reveals that the pseudoacoustic version ($g = 1$) comes closest.

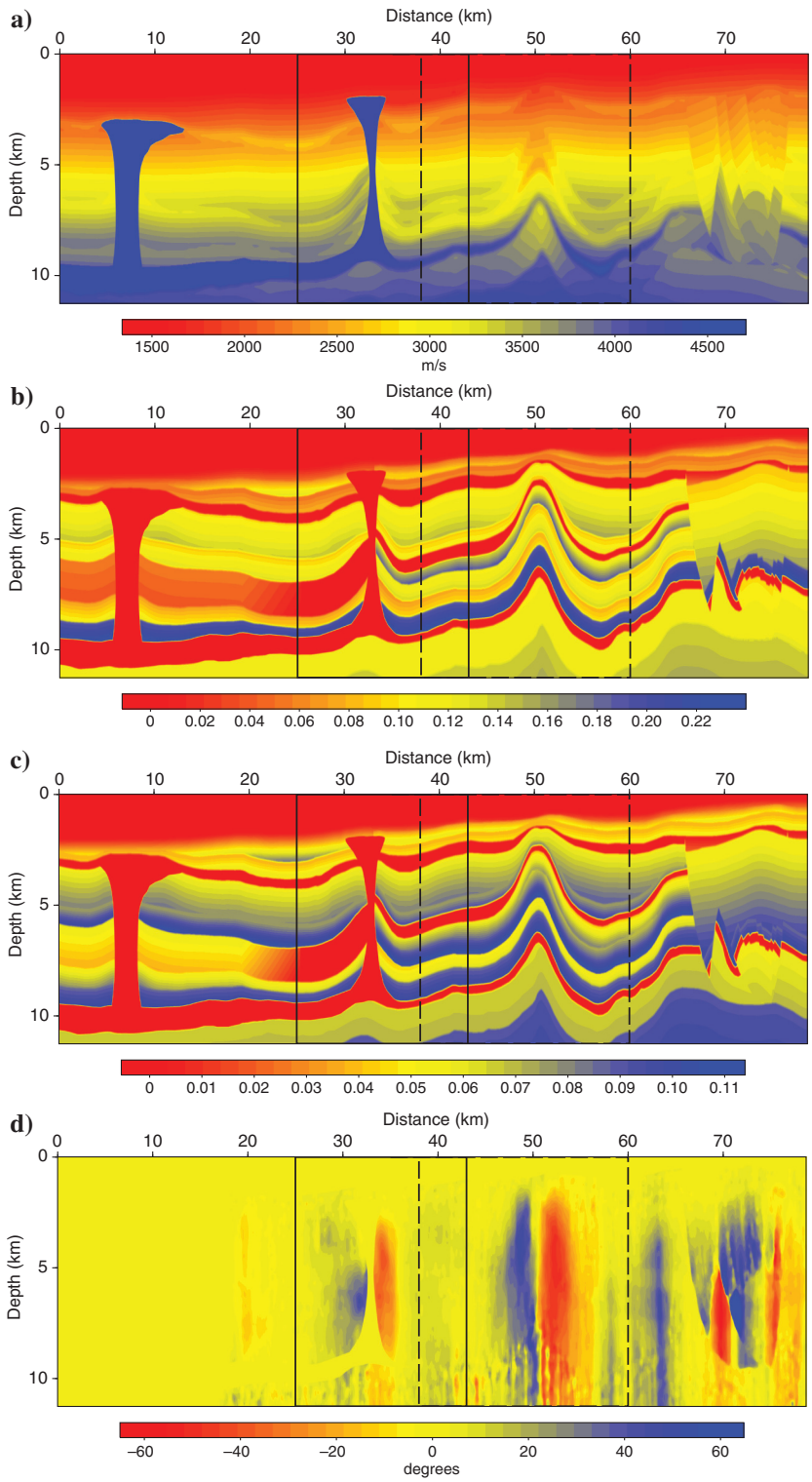

Figure 16. Model parameters of BP TTI model: (a) α, (b) ϵ, (c) δ, and (d) tilt angle. Indicated as solid and dashed boxes are the regions used for the two numerical simulations.

BP TTI model

Our final test consisted of wave simulations in the BP TTI Model (Figure 16). We simulated two shots at the surface at positions $x_s = 31.0$ and 47.0 km and restricted the model to the solid and dashed boxes, respectively, indicated in Figure 16. We chose these regions for their large variations in anisotropy parameters and tilt angle. For the second shot, we selected the region with the strongest anisotropy and most extreme tilt angles in the model. To test the approximations for even stronger anisotropy, we then repeated the second shot in a model in which we multiplied the ϵ values by a factor of two. This leads to about three times larger anellipticity.

Figures 17–19 compare snapshots of the modeled wavefields with the separable strong-anisotropy approximation to the corresponding low-rank results. We simulated the first shot at $x_s = 32.0$ km in the area indicated by the solid box in Figure 16. We observe almost perfect coincidence between the two snapshots (Figure 17). For the second shot, simulated in the area indicated by the dashed box in Figure 16, we observe a few subtle differences between the two snapshots (Figure 18). Numerical dispersion of the separable approximation is a little stronger than in the low-rank solution, resulting in slightly broadened wavelets. However, the main differences lie in the amplitude behavior. The low-rank solution suffers from stronger amplitude decay in the deeper part of the model than the separable approximation, indicating that the treatment of geometric spreading is different. Moreover, some of the reflections have visibly different amplitudes, probably caused by a different treatment of reflection and transmission coefficients. The same kind of differences, though a little more pronounced, are present in Figure 19, which compares the corresponding snapshots for the second shot position in the dashed box for the model with doubled ϵ. Regarding the amplitude differences, it should be kept in mind that these approximations of pure qP-wave propagation are meant to reproduce only the kinematic behavior and cannot be expected to predict correct elastic amplitudes.

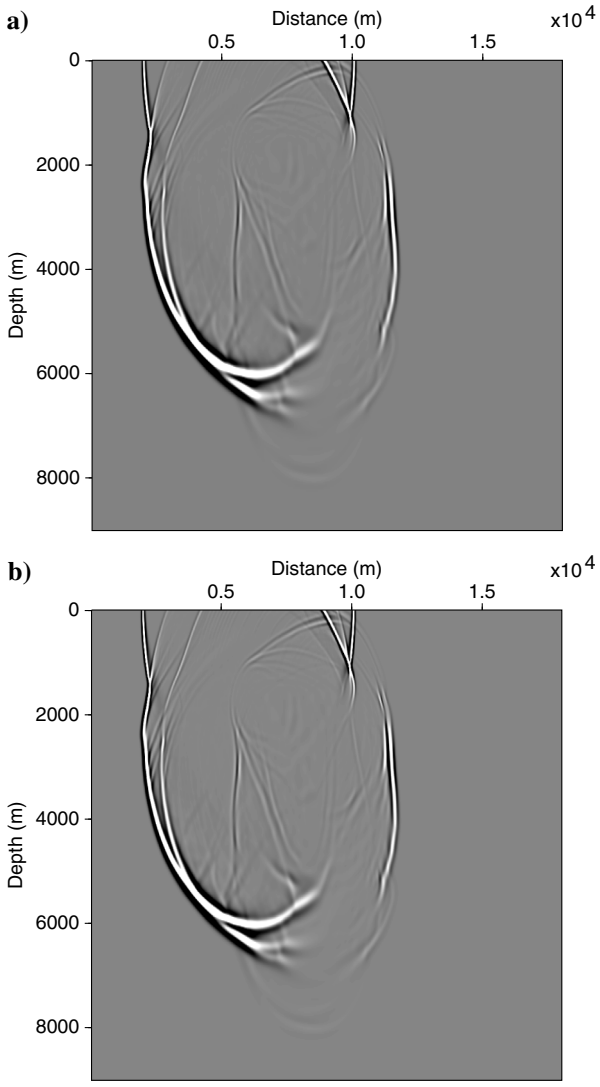

Figure 17. Snapshots at $t = 2.72$ s of qP-wave in the BP TTI model (solid-box region in Figure 16). (a) Strong-anisotropy separable approximation. (b) Low-rank approximation.

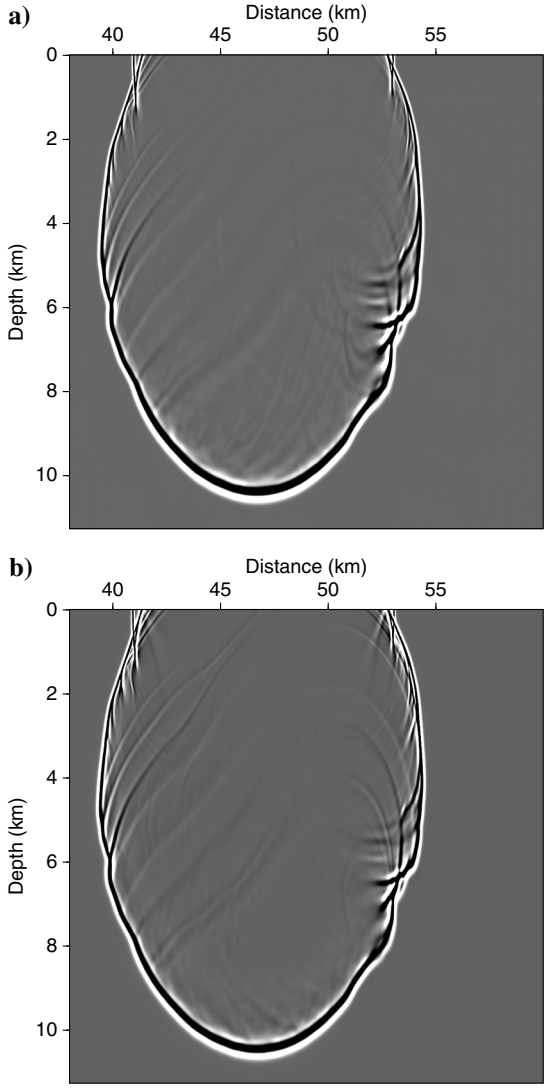

Figure 18. Snapshots at $t = 4.0$ s of qP-wave in the BP TTI model (dashed-box region in Figure 16). (a) Strong-anisotropy separable approximation. (b) Low-rank approximation.

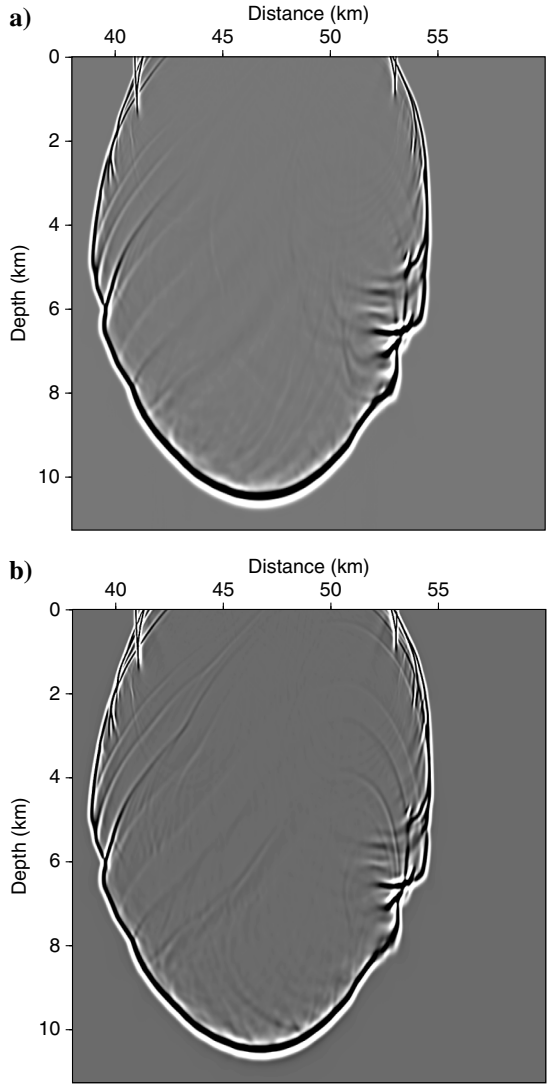

Figure 19. Snapshots at $t = 4.0$ s of qP-wave in the BP TTI model with doubled ϵ (dashed-box region in Figure 16). (a) Strong-anisotropy separable approximation. (b) Low-rank approximation.

CONCLUSIONS

We have studied elastic wave propagation in a VTI medium to better understand the coupling of qP- and qSV-wave propagation in the pseudoacoustic approximation. We have found that the pseudo-acoustic qP dispersion relation is actually a coupled equation that describes qP- and qSV-waves. The equation can be uncoupled if the individual eikonal equations are considered. Because these equations contain square roots, they cannot be directly converted into differential approximations. Even their implementation by means of a low-rank approximation might be impaired in heterogeneous and strongly anisotropic media.

Therefore, we have discussed several approximations to the square root and found that some of them have already been derived in the literature by decoupling Alkhalifah's dispersion relation. A Padé approximation with slightly unconventional, anisotropy-dependent numbers for the Padé coefficients led to a very good approximation. An implementation of a low-rank approximation to this equation demonstrated that it can provide high-accuracy wavefields even in strongly anisotropic inhomogeneous media.

Using the new equation, we derived a separable approximation that allows for pseudospectral implementation in the mixed space-wavenumber domain. This allows exploration of its potential of providing an approximation that factors heterogeneity and anisotropy even in strongly anisotropic media in the fashion used in the literature for weak anisotropy. Our numerical experiments demonstrate that this separable approximation remains valid up to very strong anisotropy. Even for extremely anisotropic biotite crystal with $\eta = 7.1875$, the slowness surface was approximated with an error of less than 5%.

Numerical modeling in the more realistic BP TTI model showed that for moderate anisotropy, the results of the new separable approximation are virtually identical to those of a low-rank solution. Increasing the anisotropy in this model, we mainly observed differences between the amplitudes. In this respect, it is important to remember that these approximations are derived to mimic the kinematic behavior of qP-waves without regard to amplitudes.

ACKNOWLEDGMENTS

This work was kindly supported by the Brazilian government agencies CAPES, FINEP, and CNPq, as well as Petrobras and the sponsors of the Wave Inversion Technology Consortium.

REFERENCES

Alkhalifah, T., 1998, Acoustic approximations for processing in transversely isotropic media: Geophysics, **63**, 623–631, doi: 10.1190/1.1444361.
Alkhalifah, T., 2000, An acoustic wave equation for anisotropic media: Geophysics, **65**, 1239–1250, doi: 10.1190/1.1444815.
Alkhalifah, T., 2003, An acoustic wave equation for orthorhombic anisotropy: Geophysics, **68**, 1169–1172, doi: 10.1190/1.1598109.
Amazonas, D., R. Aleixo, J. Schleicher, and J. C. Costa, 2010, Anisotropic complex Padé hybrid finite-difference depth migration: Geophysics, **75**, no. 2, S51–S59, doi: 10.1190/1.3337317.
Bamberger, A., B. Engquist, L. Halpern, and P. Joly, 1988, Higher order paraxial wave equation approximations in heterogeneous media: Journal on Applied Mathematics, **48**, 129–154, doi: 10.1137/0148006.
Bloot, R., J. Schleicher, and L. T. Santos, 2013, On the elastic wave equation in weakly anisotropic VTI media: Geophysical Journal International, **192**, 1144–1155, doi: 10.1093/gji/ggs066.
Červený, V., 1985, The application of ray tracing to the numerical modeling of seismic wavefields in complex structures. Part A: Theory, *in* G. Dohr, ed., Seismic shear waves: Geophysical Press, 1–124.
Červený, V., 2001, Seismic ray theory: Cambridge University Press.
Du, X., R. Fletcher, and P. J. Fowler, 2008, A new pseudo-acoustic wave equation for VTI media: 70th Annual International Conference and Exhibition, EAGE, Extended Abstracts, H033, doi: 10.3997/2214-4609.20147774.
Du, X., P. Fowler, and R. Fletcher, 2014, Recursive integral time-extrapolation methods for waves: A comparative review: Geophysics, **79**, no. 1, T9–T26, doi: 10.1190/geo2013-0115.1.
Fletcher, R., X. Du, and P. Fowler, 2009, Reverse time migration in tilted transversely isotropic (TTI) media: Geophysics, **74**, no. 6, WCA179–WCA187, doi: 10.1190/1.3269902.
Fomel, S., L. Ying, and X. Song, 2013, Seismic wave extrapolation using lowrank symbol approximation: Geophysical Prospecting, **61**, 526–536, doi: 10.1111/gpr.2013.61.issue-3.
Fowler, P., X. Du, and R. Fletcher, 2010, Coupled equations for reverse time migration in transversely isotropic media: Geophysics, **75**, no. 1, S11–S22, doi: 10.1190/1.3294572.
Grechka, V., L. Zhang, and J. Rector, 2004, Shear waves in acoustic anisotropic media: Geophysics, **69**, 576–582, doi: 10.1190/1.1707077.
Johnston, J. E., and N. I. Christensen, 1995, Seismic anisotropy of shales: Journal of Geophysical Research B, **100**, 5991–6003, doi: 10.1029/95JB00031.

Kaczmarz, S., 1993, Approximate solution of systems of linear equations: International Journal of Control, **57**, 1269–1271, doi: 10.1080/00207179308934446.

Klíe, H., and W. Toro, 2001, A new acoustic wave equation for modeling in anisotropic media: 71st Annual International Meeting, SEG, Expanded Abstracts, 1171–1174, doi: 10.1190/1.1816296.

Le, H., and S. A. Levin, 2014, Removing shear artifacts in acoustic wave propagation in orthorhombic media: 84th Annual International Meeting, SEG, Expanded Abstracts, 486–490, doi: 10.1190/segam2014-0849.1.

Liu, F., S. A. Morton, S. Jiang, L. Ni, and J. P. Leveille, 2009, Decoupled wave equations for P and SV waves in an acoustic VTI media: 79th Annual International Meeting, SEG, Expanded Abstracts, 2844–2848, doi: 10.1190/1.3255440.

Pestana, R. C., B. Ursin, and P. L. Stoffa, 2012, Rapid expansion and pseudo spectral implementation for reverse time migration in VTI media: Journal of Geophysics and Engineering, **9**, 291–301, doi: 10.1088/1742-2132/9/3/291.

Song, X., and T. Alkhalifah, 2013, Modeling of pseudoacoustic P-waves in orthorhombic media with a low-rank approximation: Geophysics, **78**, no. 4, C33–C40, doi: 10.1190/geo2012-0144.1.

Sun, J., S. Fomel, and L. Ying, 2016, Low-rank one-step wave extrapolation for reverse time migration: Geophysics, **81**, no. 1, S39–S54, doi: 10.1190/geo2015-0183.1.

Thomsen, L., 1986, Weak elastic anisotropy: Geophysics, **51**, 1954–1966, doi: 10.1190/1.1442051.

Wu, Z., and T. Alkhalifah, 2014, The optimized expansion based low-rank method for wavefield extrapolation: Geophysics, **79**, no. 2, T51–T60, doi: 10.1190/geo2013-0174.1.

Yan, J., and H. Liu, 2016, Modeling of pure acoustic wave in tilted transversely isotropic media using optimized pseudo-differential operators: Geophysics, **81**, no. 3, T91–T106, doi: 10.1190/geo2015-0111.1.

Zhan, G., R. C. Pestana, and P. L. Stoffa, 2013, An efficient hybrid pseudospectral/finite-difference scheme for solving the TTI pure p-wave equation: Journal of Geophysics and Engineering, **10**, 025004, doi: 10.1088/1742-2132/10/2/025004.

Zhou, Y., H. Wang, and W. Liu, 2015, Alternative stable qP wave equations in TTI media with their applications for reverse time migration: Journal of Geophysics and Engineering, **12**, 734–744, doi: 10.1088/1742-2132/12/5/734.